signals. In order to separate the effects of irradiation on parenchymal, Kupffere and endothelial cells, experiments involving irradiation of these cell types after cell fractionation are underway in our laboratory.

ACKNOWLEDGEMENTS

This study was supported in part by the Grants-in Aid from the Ministry of Education, Science, Sports and Culture and the Ministry of Health, Labor and Welfare of Japan. We thank Shoko Ono for her technical assistance.

REFERENCES

1. Goto, A., Takebayashi, Y., Liu, D., Li, L., Saiga, T., Mori, T., Yamadera, A. and Fukumoto, M. (2002) Microdistribution of alpha particles in pathological sections of tissues from thorotrast patients detected by imaging plate autoradiography. Radiat Res. **158**: 54–60.
2. Sharp, G. B. (2002) The relationship between internally deposited alpha-particle radiation and subsite-specific liver cancer and liver cirrhosis: an analysis of published data. J Radiat Res. **43**: 371–380.
3. Ober, S., Zerban, H., Spiethoff, A., Wegener, K., Schwarz, M. and Bannasch, P. (1994) Preneoplastic foci of altered hepatocytes induced in rats by irradiation with alpha-particles of Thorotrast and neutrons. Cancer Lett. **83**: 81–88.
4. Kopp-Schneider, A., Haertel, T., Burkholder, I., Bannasch, P., Wesch, H., Groos, J. and Heeger, S. (2006) Investigating the formation and growth of alpha-particle radiation-induced foci of altered hepatocytes: a model-based approach. Radiat Res. **166**: 422–430.
5. Yuda, T., Pongpaibul, Y., Maruyama, K. and Iwatsuru, M. (1999) Activity of Amphipathic Polyethyleneglycols to Prolong the Circulation Time of Liposomes. Journal of Pharmaceutical Science and Technology, Japan. **59**: 32–42.
6. Weichselbaum, R. R., Hallahan, D. E., Sukhatme, V., Dritschilo, A., Sherman, M. L. and Kufe, D. W. (1991) Biological consequences of gene regulation after ionizing radiation exposure. J Natl Cancer Inst. **83**: 480–484.
7. Maruyama, K., Ishida, O., Kasaoka, S., Takizawa, T., Utoguchi, N., Shinohara, A., Chiba, M., Kobayashi, H., Eriguchi, M. and Yanagie, H. (2004) Intracellular targeting of sodium mercaptoundecahydrododecaborate (BSH) to solid tumors by transferrin-PEG liposomes, for boron neutron-capture therapy (BNCT). J Control Release. **98**: 195–207.
8. Ward, J. H., (1963) Hierarchical Grouping to Optimize an Objective Function. J. Am. Statist. Assoc. **58**: 236–244.
9. McMillian, M., Nie, A. Y., Parker, J. B., Leone, A., Kemmerer, M., Bryant, S., Herlich, J., Yieh, L., Bittner, A., Liu, X., Wan, J. and Johnson, M. D. (2004) Inverse gene expression patterns for macrophage activating hepatotoxicants and peroxisome proliferators in rat liver. Biochem Pharmacol. **67**: 2141–2165.
10. Ishida, O., Maruyama, K., Sasaki, K. and Iwatsuru, M. (1999) Size-dependent extravasation and interstitial localization of polyethyleneglycol liposomes in solid tumor-bearing mice. Int J Pharm. **190**: 49–56.
11. Goldstein, I. M., Kaplan, H. B., Edelson, H. S. and Weissmann, G. (1982) Ceruloplasmin: an acute phase reactant that scavenges oxygen-derived free radicals. Ann N Y Acad Sci. **389**: 368–379.
12. Delanghe, J. R. and Langlois, M. R. (2001) Hemopexin: a review of biological aspects and the role in laboratory medicine. Clin Chim Acta. **312**: 13–23.
13. Trey, J. E. and Kushner, I. (1995) The acute phase response and the hematopoietic system: the role of cytokines. Crit Rev Oncol Hematol. **21**: 1–18.
14. Davis, S. R. and Cousins, R. J. (2000) Metallothionein expression in animals: a physiological perspective on function. J Nutr. **130**: 1085–1088.
15. Flo, T. H., Smith, K. D., Sato, S., Rodriguez, D. J., Holmes, M. A., Strong, R. K., Akira, S. and Aderem, A. (2004) Lipocalin 2 mediates an innate immune response to bacterial infection by sequestrating iron. Nature. **432**: 917–921.
16. Yanagisawa, R., Takano, H., Inoue, K., Ichinose, T., Yoshida, S., Sadakane, K., Takeda, K., Yoshino, S., Yamaki, K., Kumagai, Y. and Yoshikawa, T. (2004) Complementary DNA microarray analysis in acute lung injury induced by lipopolysaccharide and diesel exhaust particles. Exp Biol Med (Maywood). **229**: 1081–1087.
17. Lorimore, S. A., Coates, P. J., Scobie, G. E., Milne, G. and Wright, E. G. (2001) Inflammatory-type responses after exposure to ionizing radiation *in vivo*: a mechanism for radiation-induced bystander effects? Oncogene. **20**: 7085–7095.
18. Ochs, J. S. (2004) Rationale and clinical basis for combining gefitinib (IRESSA, ZD1839) with radiation therapy for solid tumors. Int J Radiat Oncol Biol Phys. **58**: 941–949.
19. Schmidt-Ullrich, R. K., Valerie, K. C., Chan, W. and McWilliams, D. (1994) Altered expression of epidermal growth factor receptor and estrogen receptor in MCF-7 cells after single and repeated radiation exposures. Int J Radiat Oncol Biol Phys. **29**: 813–819.
20. Hagan, M., Yacoub, A. and Dent, P. (2004) Ionizing radiation causes a dose-dependent release of transforming growth factor alpha *in vitro* from irradiated xenografts and during palliative treatment of hormone-refractory prostate carcinoma. Clin Cancer Res. **10**: 5724–5731.
21. Le Tourneau, C., Faivre, S. and Siu, L. L. (2007) Molecular targeted therapy of head and neck cancer: Review and clinical development challenges. Eur J Cancer.
22. Donnellan, R. and Chetty, R. (1999) Cyclin E in human cancers. Faseb J. **13**: 773–780.
23. Moroy, T. and Geisen, C. (2004) Cyclin E. Int J Biochem Cell Biol. **36**: 1424–1439.
24. Arlett, C. F., Plowman, P. N., Rogers, P. B., Parris, C. N., Abbaszadeh, F., Green, M. H., McMillan, T. J., Bush, C., Foray, N. and Lehmann, A. R. (2006) Clinical and cellular ionizing radiation sensitivity in a patient with xeroderma pigmentosum. Br J Radiol. **79**: 510–517.
25. Juncker-Jensen, A., Lykkesfeldt, A. E., Worm, J., Ralfkiaer, U., Espelund, U. and Jepsen, J. S. (2006) Insulin-like growth factor binding protein 2 is a marker for antiestrogen resistant human breast cancer cell lines but is not a major growth regulator. Growth Horm IGF Res. **16**: 224–239.

26. Dunlap, S. M., Celestino, J., Wang, H., Jiang, R., Holland, E. C., Fuller, G. N. and Zhang, W. (2007) Insulin-like growth factor binding protein 2 promotes glioma development and progression. Proc Natl Acad Sci USA. **104**: 11736–11741.
27. Gao, D., Wei, C., Chen, L., Huang, J., Yang, S. and Diehl, A. M. (2004) Oxidative DNA damage and DNA repair enzyme expression are inversely related in murine models of fatty liver disease. Am J Physiol Gastrointest Liver Physiol. **287**: G1070–1077.
28. Mercier, G., Berthault, N., Mary, J., Peyre, J., Antoniadis, A., Comet, J. P., Cornuejols, A., Froidevaux, C. and Dutreix, M. (2004) Biological detection of low radiation doses by combining results of two microarray analysis methods. Nucleic Acids Res. **32**: e12.
29. Paris, F., Fuks, Z., Kang, A., Capodieci, P., Juan, G., Ehleiter, D., Haimovitz-Friedman, A., Cordon-Cardo, C. and Kolesnick, R. (2001) Endothelial apoptosis as the primary lesion initiating intestinal radiation damage in mice. Science. **293**: 293–297.

Received on August 16, 2007
Revision received on October 11, 2007
Accepted on October 18, 2007
J-STAGE Advance Publication Date: November 30, 2007

Novel SN-38–Incorporated Polymeric Micelle, NK012, Strongly Suppresses Renal Cancer Progression

Makoto Sumitomo,[1] Fumiaki Koizumi,[2] Takako Asano,[1] Akio Horiguchi,[1] Keiichi Ito,[1] Tomohiko Asano,[1] Tadao Kakizoe,[3] Masamichi Hayakawa,[1] and Yasuhiro Matsumura[4]

[1]Department of Urology, National Defense Medical College, Tokorozawa, Saitama, Japan; [2]Shien-Lab, Medical Oncology, National Cancer Center Hospital; [3]National Cancer Center, Tokyo, Japan; and [4]Investigative Treatment Division, Research Center for Innovative Oncology, National Cancer Center Hospital East, Chiba, Japan

Abstract

It has been recently reported that NK012, a 7-ethyl-10-hydroxy-camptothecin (SN-38)–releasing nanodevice, markedly enhances the antitumor activity of SN-38, especially in hypervascular tumors through the enhanced permeability and retention effect. Renal cell carcinoma (RCC) is a typical hypervascular tumor with an irregular vascular architecture. We therefore investigated the antitumor activity of NK012 in a hypervascular tumor model from RCC. Immunohistochemical examination revealed that Renca tumors contained much more CD34-positive neovessels than SKRC-49 tumors. Compared with CPT-11, NK012 had significant antitumor activity against both bulky Renca and SKRC-49 tumors. Notably, NK012 eradicated rapid-growing Renca tumors in 6 of 10 mice, whereas it failed to eradicate SKRC-49 tumors. In the pulmonary metastasis treatment model, an enhanced and prolonged distribution of free SN-38 was observed in metastatic lung tissues but not in nonmetastatic lung tissues after NK012 administration. NK012 treatment resulted in a significant decrease in metastatic nodule number and was of benefit to survival. Our study shows the outstanding advantage of polymeric micelle-based drug carriers and suggests that NK012 would be effective in treating disseminated RCCs with irregular vascular architectures. [Cancer Res 2008;68(6):1631–5]

Introduction

Passive targeting of the drug delivery system is suited to combating the pathophysiologic characteristics present in many solid tumors: hypervascularity, irregular vascular architecture, potential for secretion of vascular permeability factors, and the absence of effective lymphatic drainage that prevents efficient clearance of macromolecules. These characteristics, unique to solid tumors, are believed to be the basis of the enhanced permeability and retention (EPR) effect (1). Polymeric micelle-based anticancer drugs have recently been developed (2, 3), and some were put under evaluation for clinical trials (4, 5).

7-Ethyl-10-hydroxy-camptothecin (SN-38), a biological active metabolite of irinotecan hydrochloride (CPT-11), has potent antitumor activity, but has not been used clinically because it is a water-insoluble drug. It has been recently shown that novel SN38-incorporated polymeric micelles, NK012, have the potential to allow effective sustained release of SN-38 inside a tumor and possess potent antitumor activities especially in a vascular endothelial growth factor (VEGF)–secreting hypervascular tumor (6), because the supramolecular structures of NK012 which enable SN-38 to accumulate in the target tissue are based on the EPR effect (1).

Renal cell carcinoma (RCC) is a typical hypervascular tumor with an irregular vascular architecture. We therefore conducted an investigation to determine whether NK012 would be effective in treating RCC by using established RCC tumor models with pulmonary metastasis.

Materials and Methods

Drugs and cells. CPT-11 was purchased from Yakult Honsha Co., Ltd. SN-38 and NK012 was prepared and supplied by Nippon Kayaku Co., Ltd. (6). Five human RCC lines (SKRC-49, Caki-1, 769P, 786O, and KU19-20) and murine Renca cells were maintained in DMEM or MEM supplemented with 2 mmol/L glutamine, 1% nonessential amino acids, 100 units/mL streptomycin and penicillin, and 10% FCS.

***In vitro* growth inhibition assay.** The growth inhibitory effects of NK012, SN-38, and CPT-11 were examined with a 3-(4, 5-dimethylthiazol-2-yl)-2, 5-diphenyltetrazolium bromide (MTT) assay, as described previously (6).

***In vivo* growth inhibition assay.** The animal experimental protocols were approved by the Committee for Ethics of Animal Experimentation, and the experiments were conducted in accordance with the Guidelines for Animal Experiments in the National Cancer Center. Athymic nude mice (3–4 wk old) were maintained in a laminar air flow cabinet under aseptic conditions. 10^7 RCC cells were s.c. injected into the backs of the mice. NK012 at doses of 10 mg/kg/d or 20 mg/kg/d and CPT-11 at doses of 15 mg/kg/d or 30 mg/kg/d were given i.v. on days 0 (when tumors were allowed to grow until they became massive in size, around 1.5 cm), 4, and 8. Tumor volume was determined by direct measurement with calipers and calculated as $\pi/6 \times (\text{large diameter}) \times (\text{small diameter})^2$.

Assessment of treatment effects of NK012 on murine pulmonary metastasis model. A total of 1×10^5 Renca cells were inoculated into male BALB/c mice via the tail vein. The mice were randomly divided into three groups of 10. NK012 at dose of 20 mg/kg/d and CPT-11 at dose of 30 mg/kg/d were given i.v. on days 0 (7 d after inoculation), 4, and 8. After that, the mice were sacrificed, their lungs were stained intratracheally with 15% India black ink solution, and the number of metastatic nodules in each mouse was counted. To determine the effect of NK012 on survival, an identical experiment to the one described above was done. After treatment, mice were maintained until each animal showed signs of morbidity (i.e., over 10% weight loss compared with untreated controls), at which point they were sacrificed. Kaplan-Meier analysis was done to determine the effect on time to morbidity, and statistical differences were ranked according to a Mantel-Cox log-rank test using the StatView 5.0 software package.

Histologic and immunohistochemical analysis. Histologic sections were taken from Renca tumor tissues. After extirpation, tissues were fixed with 3.9% formalin in PBS (pH 7.4), and the subsequent preparations and H&E staining were performed by Tokyo Histopathological Laboratory Co.,

Requests for reprints: Yasuhiro Matsumura, Investigative Treatment Division, Research Center for Innovative Oncology, National Cancer Center Hospital East, 6-5-1 Kashiwanoha, Kashiwa City, Chiba 277-8577, Japan. Phone: 81-4-7134-6857; Fax: 81-4-7134-6857; E-mail: yhmatsum@east.ncc.go.jp.

doi:10.1158/0008-5472.CAN-07-6532

Table 1. *In vitro* growth inhibitory activity of SN-38, NK012, and CPT-11 in RCC lines (MTT assay)

Cell line	IC_{50} (μmol/L)		
	SN-38	NK012*	CPT-11
SKRC-49	0.0064 ± 0.005	0.011 ± 0.008	4.14 ± 0.45
Caki-1	0.0062 ± 0.009	0.032 ± 0.006	8.45 ± 0.85
769P	0.015 ± 0.007	0.085 ± 0.014	34.54 ± 3.76
786O	0.031 ± 0.007	0.12 ± 0.012	28.14 ± 1.21
KU19-20	0.10 ± 0.006	0.34 ± 0.014	32.65 ± 1.25
Renca	0045 ± 0.005	0.0096 ± 0.008	2.26 ± 0.05

*The dose of NK012 is expressed as a dose equivalent to SN-38.

Ltd. Monoclonal anti-CD34 antibody (HyCult Biotechnology) was used to detect the tumor blood vessels. CD34-positive neovessels were counted in 10 high-power fields (×400) by two independent investigators who operated in a blinded fashion.

Assay for free (polymer-unbound) SN-38 in lung tissues. The Renca pulmonary metastasis model described above was used for the analysis of the biodistribution of NK012 and CPT-11. Ten days after Renca inoculation, NK012 (20 mg/kg) or CPT-11 (30 mg/kg) was given i.v. to the mice. The mice were sacrificed at 0, 24, 48, and 72 h after administration, and lung samples were taken and stored at −80°C until analysis. We prepared control mice without Renca inoculation as the nonmetastatic model; NK012 was administrated as well, and lung samples were stored. Samples were then homogenized on ice using a Digital homogenizer (Iuchi) and suspended in the mixture of 100 mmol/L glycine-HCl buffer (pH 3)/methanol (1:1, v/v) at a concentration of 5% w/w. Proteins were precipitated with an ice-cold mixture of 1 mmol/L H_3PO_4/MeOH/H_2O (1:1:4, v/v/v) containing camptothecin as an I.S. The sample was vortexed for 10 s and filtered through a MultiScreen Solvinert (Millipore Corporation), and the concentration of free SN-38 in the aliquots of the homogenates (100 μL) was determined using the high-performance liquid chromatography method (6).

Statistical analysis. Data were expressed as mean ± SD. Significance of differences was calculated using the unpaired *t* test with repeated measures of StatView 5.0. $P < 0.05$ was regarded as statistically significant.

Results and Discussion

We first evaluated *in vitro* cellular sensitivity of RCC lines to SN-38, NK012, and CPT-11. The IC_{50} values of each agent for RCC lines are shown in Table 1. NK012 exhibited higher cytotoxic effect against each cell line compared with CPT-11 (96-fold to 406-fold sensitive).

It is essential to elucidate the correlation between the effectiveness of micellar drugs and tumor hypervascularity and hyperpermeability. Gross evaluation of those RCC tumors s.c. injected into the backs of mice revealed that Renca tumors were more reddish and grew faster than SKRC-49 tumors, and immunohistochemical examination showed that Renca tumors contained much more CD34-positive neovessels than SKRC-49 tumors (Fig. 1).

We allowed the tumors to grow until they became massive, around 1.5 cm, and then initiated treatment. A striking decrease in Renca tumor volume was observed on day 15 in mice treated with NK012 at 20 mg/kg/d compared with the untreated control (Fig. 2*A*). Renca bulky masses completely disappeared on day 21 in 6 of 10 mice treated with NK012 at 20 mg/kg/d. On the other hand, Renca tumors in mice treated with CPT-11 at 30 mg/kg/d were not eradicated and rapidly regrew after a partial response at day 15. An approximate 10% body weight loss occurred in mice treated with NK012 20 mg/kg, compared with the untreated controls, but there was no significant difference in comparison with tumor-free mice treated with NK012, suggesting that the decrease in body weight was likely to be due to tumor shrinkage rather than toxic effects. We next compared the antitumor activities of the NK012 and CPT-11 treatment in SKRC-49 and Renca tumors. The SKRC-49 tumor volume in mice treated with NK012 at 20 mg/kg/d on day 21 was over 70% smaller than in the untreated controls on day 21 and −50% smaller than in mice on day 0 (Fig. 2*B*). However, the SKRC-49 tumors were not eradicated in mice treated with NK012. Considering that equivalent *in vitro* growth inhibitory effects by NK012 were observed for SKRC-49 and Renca cells (Table 1), our results suggest that the antitumor activity of NK012 *in vivo* might be affected by tumor environment factors, such as tumor vascularity.

We next examined the distribution of free SN-38 in the metastatic or nonmetastatic (no inoculation of Renca cells) lung tissues after administration of NK012 or CPT-11. In the case of NK012 administration in mice with lung metastasis, free SN-38 was detectable at the concentration of >100 ng/g in metastatic lung tissues with a typical microvascular architecture (Fig. 3*A*) even at 72 hours after administration, whereas the concentrations of free SN-38 in nonmetastatic lung tissues after NK012 administration were much lower than those in metastatic lung tissues after treatment with NK012 (significant at 24, 48, and 72 hours; $P < 0.05$;

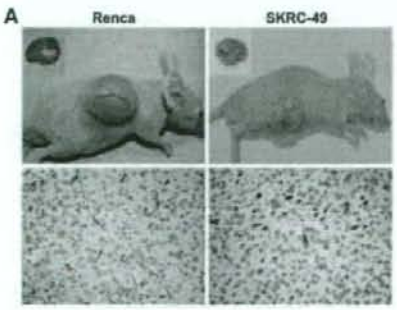

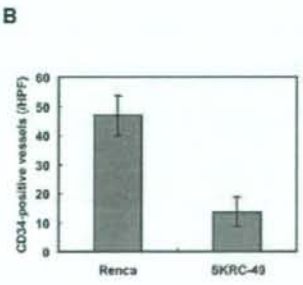

Figure 1. Comparison of tumor angiogeneses of Renca and SKRC-49 in athymic nude mice. *A*, representative photographs of massive tumors developed from Renca and SKRC-49 at 28 d after s.c. injection (inoculation). Immunohistochemical (CD34, ×400) examinations for each tumor are shown. *B*, tumor neovascularization in each tumor was quantified by counting CD34-positive neovessels. *Bars*, SD. Experiments were repeated twice with similar results.

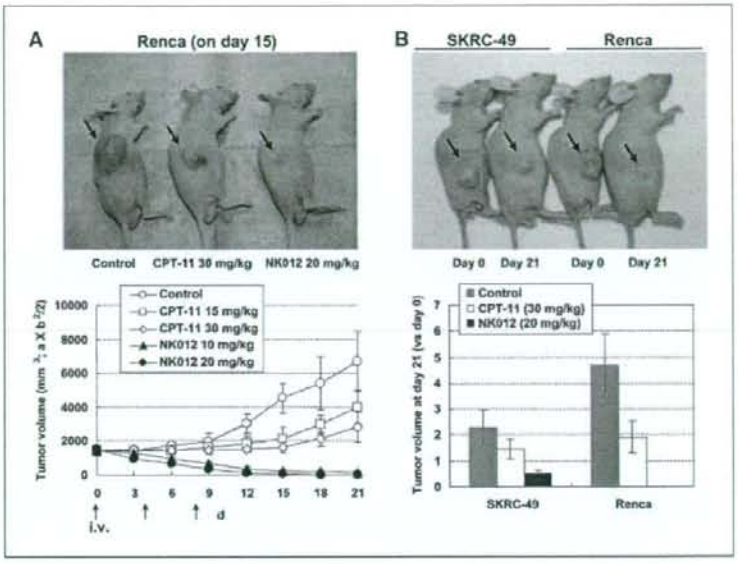

Figure 2. Growth-inhibitory effect of NK012 and CPT-11 on bulky RCC tumors. I.v. administration of NK012 or CPT-11 was started when the mean tumor volumes of groups reached a massive 1,500 mm^3. The mice were divided into test groups as indicated. *A*, representative of each group at day 15 in the Renca allograft model. *Arrows*, Renca allografts (*top*). Time profile of tumor volume in mice treated with NK012 or CPT-11 at indicated doses (*bottom*). Each group consisted of 10 mice. *Bars*, SD. *B*, the comparison of antitumor activities of CPT-11 and NK012 in SKRC-49 xenografts and Renca allografts. Representative of mice treated with NK012 at day 0 and day 21. Experiments were repeated twice with similar results. The mice at day 0 in the photograph belong to the group in the second experiment which started just at day 21 of the first experiment. *Arrows*, tumor grafts. The relative tumor volume values at day 21 to those at day 0 in each group set to 1 (*bottom*). Each group consisted of 10 mice.

Fig. 3*B*). On the other hand, the concentrations of free SN-38 after administration of CPT-11 were almost negligible in metastatic lung tissues at all time points (data not shown). These results strongly suggest that SN-38 could be selectively released from NK012 and maintained in metastatic Renca tumor tissues.

Deviating from the ordinary experimental pulmonary metastasis prevention model, we initiated treatment 7 days after inoculation (day 0) when multiple lung nodules derived from Renca were observed in all mice in our preliminary study (Fig. 4*A*). On day 21, there was no significant difference between the mean number of metastatic nodules in the control group (287 ± 56 nodules, $n = 10$) and in the group receiving CPT-11 treatment (236 ± 59 nodules, $n = 10$). Significant treatment effects were found, however, in the group receiving NK012 treatment (32 ± 18 nodules, $n = 10$) on day 21 compared with the control group on day 21 ($P < 0.0001$). Notably, a dramatic decrease in metastatic nodule number was observed in the NK012 treatment group on day 21 compared with the control group on day 0 (126 ± 23 nodules, $n = 10$, $P < 0.001$; Fig. 4*A*). Kaplan-Meier analysis showed that a significant survival benefit was obtained in the NK012 treatment group compared with

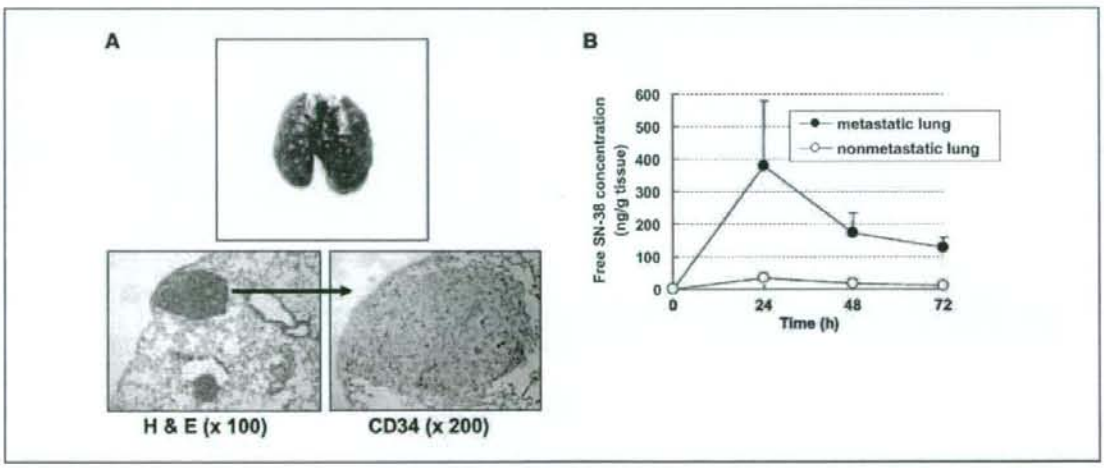

Figure 3. Pulmonary metastasis of Renca cells and lung tissue distribution of free SN-38 after administration of NK012 and CPT-11. *A*, gross appearances of pulmonary metastasis observed 7 d after Renca inoculation (*top*). Multiple metastatic nodules and neovascularization in metastatic lung tumor lesion (*bottom*). *B*, time profile of free SN-38 concentration in metastatic or nonmetastatic lung tissues in mice treated with NK012 (20 mg/kg/d). *Bars*, SD. Experiments were performed in tetraplicate.

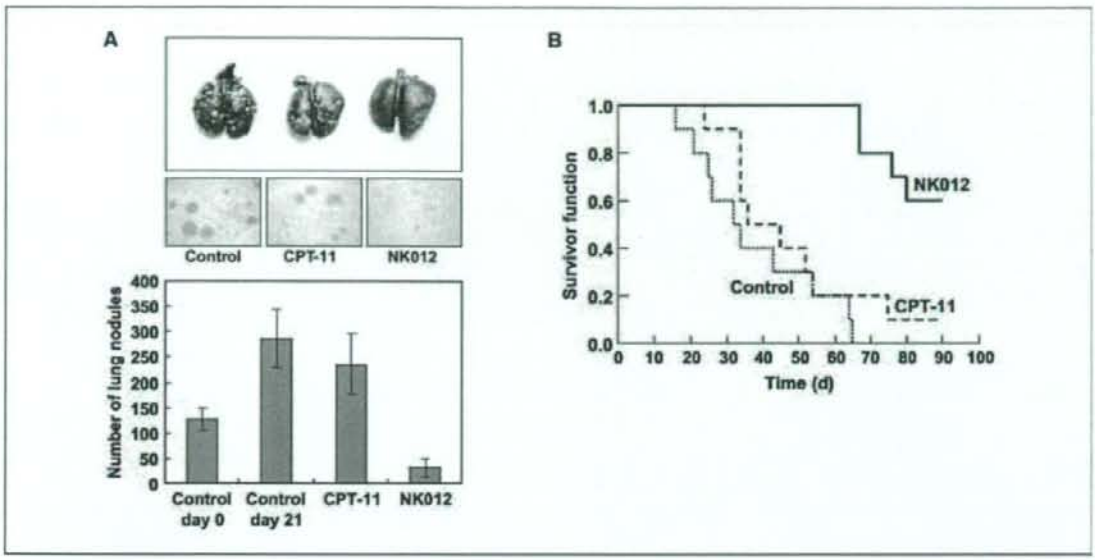

Figure 4. Treatment effect of NK012 on established pulmonary metastasis and survival. NK012 (20 mg/kg/d) and CPT-11 (30 mg/kg/d) were given i.v. to mice with established pulmonary metastasis on days 0 (7 d after Renca inoculation), 4, and 8. *A*, gross and histologic appearances of pulmonary metastases at day 21 (*top*). The metastatic nodules in each mouse were counted. Each group consisted of five mice. *B*, mice were maintained for 90 d after each treatment and survival was assessed by a Kaplan-Meier analysis. Each group consisted of five mice. Experiments were repeated twice with similar results.

the control group ($P < 0.001$), but no significant survival benefit was obtained in CPT-11 treatment group ($P = 0.239$; Fig. 4*B*). Although no severe toxic effects were observed in any mouse treated with NK012, 3 of 10 mice treated with NK012 were sacrificed during the observation period according to the 'Guidelines for Animal Experiments because their body weights had become 10% lower than those of the other mice. However, the sacrificed mice were a little bit smaller than others when they started treatment, and they showed no disseminated lung metastasis (data not shown).

Our results presented here strongly support recent findings reported by us that the macromolecular drug distribution throughout the tumor site was enhanced by the hypervascularity and hyperpermeability, and subsequently higher antitumor activity was achieved (6). We assume that conventional low molecular size anticancer agents almost disappear from the bloodstream without being subjected to the EPR effect before they can reach the target organs (solid tumor). The clinical importance of angiogenesis in human tumors has been shown in several reports indicating a positive relationship between the blood vessel density in the tumor mass and poor prognosis with chemoresistance in patients with various cancers (7–9). Furthermore, recent reports showing that anticancer agents were less active against VEGF-overexpressing tumors (10, 11) may support the idea that low-molecular drugs are not so effective in the treatment of solid tumors which are rich in blood vessels.

Our study thus far has several limitations about clarifying whether extensive angiogenesis in the tumor is an essential determinant for the susceptibility to NK012. In our ongoing study, we found that NK012 also has a striking antitumor activity against some hypovascular tumor models of human pancreatic cancer xenografts.[5] It also remains unclear whether NK012 possesses strong antitumor activity in other metastatic sites besides the lung. It is known that the EPR effect is affected by various permeability factors, such as bradykinin (12), nitric oxide (13), and various cytokines independent of VEGF and hypervascularity (14). Among solid tumors with rapid progression potential, irregularity occurs not only in blood flow and vascular density, but also in the vascular network and anatomic architecture (15, 16), suggesting that EPR effect may be predominantly promoted in rapid-progressive tumor phenotypes and influenced by organ-specific tumor microenvironment. Hoffman and coworkers (17, 18) have developed a technique of surgical orthotopic implantation (SOI) with more clinical features of systemic and aggressive metastases than our conventional animal models. Further preclinical studies using such models as SOI might clarify cancer phenotypes and metastatic organs to which we can apply NK012 more precisely.

The results of chemotherapy in RCCs have been disappointing, as indicated by the low response proportions. However, clinical trials using gemcitabine-containing regimens have been encouraging, with major responses occurring in 5% to 17% of patients (19, 20), suggesting the possibility that chemotherapy is promising as a modality for RCC therapy if anticancer agents can be selectively delivered, released, and maintained around tumor tissues. Our current report highlights the advantages of polymeric micelle-based drug carriers like NK012 as promising modalities for treatment, rather than prevention, of disseminated RCCs with abnormal vascular architecture. The results of our ongoing phase-I

[5] Y. Saito, M. Yasumaga, J. Kuroda, Y. Koga, and Y. Matsumura. Unpublished data.

clinical trial and future phase-II trials of NK012 in patients with advanced solid tumors including RCC might meet or even exceed our expectations.

Acknowledgments

Received 12/10/2007; revised 1/25/2008; accepted 1/31/2008.

Grant support: Grant-in-aid from 3rd Term Comprehensive Control Research for Cancer, Ministry of Health, Labor and Welfare (Y. Matsumura) and Scientific Research on Priority Areas from the Ministry of Education, Culture, Sports, Science and Technology (Y. Matsumura).

The costs of publication of this article were defrayed in part by the payment of page charges. This article must therefore be hereby marked *advertisement* in accordance with 18 U.S.C. Section 1734 solely to indicate this fact.

We thank H. Miyatake and N. Mie for their technical assistance and K. Shiina for her secretarial assistance.

References

1. Matsumura Y, Maeda H. A new concept for macromolecular therapeutics in cancer chemotherapy: mechanism of tumoritropic accumulation of proteins and the antitumor agent smancs. Cancer Res 1986;46:6387–92.
2. Yokoyama M, Miyauchi M, Yamada N, et al. Characterization and anticancer activity of the micelle-forming polymeric anticancer drug adriamycin-conjugated poly(ethylene glycol)-poly(aspartic acid) block copolymer. Cancer Res 1990;50:1693–700.
3. Kataoka K, Harada A, Nagasaki Y. Block copolymer micelles for drug delivery: design, characterization and biological significance. Adv Drug Deliv Rev 2001;47:113–31.
4. Matsumura Y, Hamaguchi T, Ura T, et al. Phase I clinical trial and pharmacokinetic evaluation of NK911, a micelle-encapsulated doxorubicin. Br J Cancer 2004;91:1775–81.
5. Hamaguchi T, Kato K, Yasui H, et al. A phase I and pharmacokinetic study of NK105, a paclitaxel-incorporating micellar nanoparticle formulation. Br J Cancer 2007;97:170–6.
6. Koizumi F, Kitagawa M, Negishi T, et al. Novel SN-38-incorporating polymeric micelles, NK012, eradicate vascular endothelial growth factor-secreting bulky tumors. Cancer Res 2006;66:10048–56.
7. Gasparini G, Harris AL. Clinical importance of the determination of tumor angiogenesis in breast carcinoma: much more than a new prognostic tool. J Clin Oncol 1995;13:765–82.
8. Takahashi Y, Kitadai Y, Bucana CD, Cleary KR, Ellis LM. Expression of vascular endothelial growth factor and its receptor, KDR, correlates with vascularity, metastasis, and proliferation of human colon cancer. Cancer Res 1995;55:3964–8.
9. Williams JK, Carlson GW, Cohen C, Derose PB, Hunter S, Jurkiewicz MJ. Tumor angiogenesis as a prognostic factor in oral cavity tumors. Am J Surg 1994;168:373–80.
10. Natsume T, Watanabe J, Koh Y, et al. Antitumor activity of TZT-1027 (Soblidotin) against vascular endothelial growth factor-secreting human lung cancer *in vivo*. Cancer Sci 2003;94:826–33.
11. Zhang L, Hannay JA, Liu J, et al. Vascular endothelial growth factor overexpression by soft tissue sarcoma cells: implications for tumor growth, metastasis, and chemoresistance. Cancer Res 2006;66:8770–8.
12. Matsumura Y, Maruo K, Kimura M, Yamamoto T, Konno T, Maeda H. Kinin-generating cascade in advanced cancer patients and *in vitro* study. Jpn J Cancer Res 1991;82:732–41.
13. Wu J, Akaike T, Hayashida K, et al. Identification of bradykinin receptors in clinical cancer specimens and murine tumor tissues. Int J Cancer 2002;98:29–35.
14. Maeda H, Fang J, Inutsuka T, Kitamoto Y. Vascular permeability enhancement in solid tumor: various factors, mechanisms involved and its implications. Int Immunopharmacol 2003;3:319–28.
15. Suzuki M, Takahashi T, Sato T. Medial regression and its functional significance in tumor-supplying host arteries. A morphometric study of hepatic arteries in human livers with hepatocellular carcinoma. Cancer 1987;59:444–50.
16. Skinner SA, Tutton PJ, O'Brien PE. Microvascular architecture of experimental colon tumors in the rat. Cancer Res 1990;50:2411–7.
17. An Z, Jiang P, Wang X, Moossa AR, Hoffman RM. Development of a high metastatic orthotopic model of human renal cell carcinoma in nude mice: benefits of fragment implantation compared to cell-suspension injection. Clin Exp Metastasis 1999;17:265–70.
18. Hoffman RM. Orthotopic metastatic mouse models for anticancer drug discovery and evaluation: a bridge to the clinic. Invest New Drugs 1999;17:343–59.
19. Rini BI, Vogelzang NJ, Dumas MC, Wade JL III, Taber DA, Stadler WM. Phase II trial of weekly intravenous gemcitabine with continuous infusion fluorouracil in patients with metastatic renal cell cancer. J Clin Oncol 2000;18:2419–26.
20. Nanus DM, Garino A, Milowsky MI, Larkin M, Dutcher JP. Active chemotherapy for sarcomatoid and rapidly progressing renal cell carcinoma. Cancer 2004;101:1545–51.

Available online at www.sciencedirect.com
ScienceDirect
Journal of Controlled Release 125 (2008) 137–144
journal of controlled release
www.elsevier.com/locate/jconrel
GENE DELIVERY

Tumor specific ultrasound enhanced gene transfer *in vivo* with novel liposomal bubbles

Ryo Suzuki [a], Tomoko Takizawa [a], Yoichi Negishi [b], Naoki Utoguchi [a], Kaori Sawamura [a], Kumiko Tanaka [a], Eisuke Namai [a], Yusuke Oda [a], Yasuhiro Matsumura [c], Kazuo Maruyama [a,*]

[a] *Department of Biopharmaceutics, School of Pharmaceutical Sciences, Teikyo University, 1091-1 Suwarashi, Sagamiko, Sagamihara, Kanagawa 229-0195, Japan*
[b] *Department of Drug and Gene Delivery System, School of Pharmacy, Tokyo University of Pharmacy and Life Science, Hachioji, Tokyo, Japan*
[c] *Investigative Treatment Division, Research Center for Innovative Oncology, National Cancer Center Hospital East, Kashiwa, Chiba, Japan*

Received 30 November 2006; accepted 19 August 2007
Available online 29 August 2007

Abstract

Bubble liposomes (liposomes which entrap an ultrasound imaging gas) may constitute a unique system for delivering various molecules efficiently into mammalian cells *in vitro*. In this study, Bubble liposomes were compared with cationic lipid (CL)–DNA complexes as potential gene delivery carriers into tumor *in vivo*. The delivery of genes by Bubble liposomes depended on the intensity of the applied ultrasound. Transfection efficiency plateaued at 0.7 W/cm^2 ultrasound intensity. Bubble liposomes efficiently transferred genes into cultured cells even when the cells were exposed to ultrasound for only 1 s. In addition, Bubble liposomes could introduce the luciferase gene more effectively than CL-DNA complexes into mouse ascites tumor cells and solid tumor tissue. We conclude that the combination of Bubble liposomes and ultrasound is a minimally-invasive and tumor specific gene transfer method *in vivo*.

Keywords: Liposomes; Bubble liposomes; Gene delivery; Ultrasound; Cancer

1. Introduction

In cancer gene therapy, it is important to develop the easy, safe, efficient, minimally-invasive and tissue-specific technologies of gene transfer into tumor tissue. Sonoporation is a method of gene delivery with ultrasound. Ultrasound increases the permeability of the plasma membrane and reduces the thickness of the unstirred layer of the cell surface, aiding DNA entry into cells [1,2]. Preliminary studies into the utility of ultrasound for gene delivery used frequencies in the range of 20–50 kHz [1,3]. However, these frequencies are also known to induce tissue damage and cavitation if not properly controlled [4–6]. To overcome this problem, several studies have used frequencies of 1–3 MHz, intensities of 0.5–2 W/cm^2, and pulse-modulation [7–9]. In a separate approach, a combination of therapeutic ultrasound and microbubble echo contrast agents was shown to enhance gene transfection efficiency [10–15] by effectively and directly transferring DNA into the cytosol. Microbubbles based on protein microspheres, and sugar microbubbles, are commercially available; however, although they encapsulate ultrasound contrast agents, they are too large (2–10 μm diameter) for intravascular application [16]. It has been reported that the *i.v.* injection of Optison without ultrasound exposure results in lethal embolisms in vital organs in mice [17]. Although a similar effect has not been observed in humans, it is possible that Optison can not pass through capillary vessels. Ideally, microbubbles should be smaller than red blood cells.

Liposomes can be used as drug, antigen and gene delivery carriers [18–26]. Based on liposome technology, we developed novel liposomal bubbles (Bubble liposomes) containing the ultrasound imaging gas, perfluoropropane. When coupled with ultrasound exposure, Bubble liposomes can be used as novel

* Corresponding author. Tel.: +81 42 685 3722; fax: +81 42 685 3432.
E-mail address: maruyama@pharm.teikyo-u.ac.jp (K. Maruyama).

0168-3659/$ - see front matter © 2007 Elsevier B.V. All rights reserved.
doi:10.1016/j.jconrel.2007.08.025

gene delivery agents [27]. In addition, we found out that the gene delivery was only observed at the site of ultrasound exposure. Therefore, using Bubble liposomes and ultrasound, we could establish minimally-invasive and tumor tissue-specific gene delivery. In the present study, the characteristics of Bubble liposomes as gene delivery vectors were studied, and gene transfection efficiencies into tumor *in vivo* were compared with lipofection using cationic liposomes, a common non-viral gene transfer method.

2. Materials and methods

2.1. Cells

African green monkey kidney fibroblast COS-7 cells were cultured in Dulbecco's modified Eagle's medium (DMEM; Sigma Chemical Co., St. Louis, MO) supplemented with 10% heat inactivated fetal Bovine serum (FBS, GIBCO, Invitrogen Co., Carlsbad, CA). Mouse Sarcoma-180 (S-180) cells were cultured in Eagle's medium (MEM; Sigma) supplemented with 10% heat inactivated FBS. All culture media contained 100 U/mL penicillin (Wako Pure Chemical Industries, Ltd., Osaka, Japan) and 100 μg/mL streptomycin (Wako).

2.2. Preparation of liposomes and Bubble liposomes

Liposomes composed of 1,2-distearoyl-sn-glycero-phosphatidylcholine (DSPC) (NOF Corporation, Tokyo, Japan) and 1,2-distearoyl-sn-glycero-3-phosphatidyl-ethanolamine-methoxy-polyethyleneglycol (DSPE-PEG (2 k)–OMe; NOF) (94:6 (m/m)) were prepared by reverse phase evaporation. In brief, all reagents (total lipid: 100 μmol) were dissolved in 8 mL of 1:1 (v/v) chloroform/diisopropyl ether, then 4 mL of PBS was added. The mixture was sonicated and evaporated at 65 °C. The solvent was completely removed, and the size of the liposomes was adjusted to less than 200 nm using an extruding apparatus (Northern Lipids Inc., Vancouver, BC) and sizing filters (pore sizes: 100 nm and 200 nm; Nuclepore Track-Etch Membrane, Whatman plc, UK). After sizing, the liposomes were sterilized by passing them through a 0.45 μm pore size filter (MILLEX HV filter unit, Durapore PVDF membrane, Millipore Corporation, MA). The liposome size was measured with dynamic light scattering (ELS-800, Otsuka Electronics Co., Ltd., Osaka, Japan). The average diameter of these liposomes were about 150–200 nm. Lipid concentration was measured with the Phospholipid C test wako (Wako Pure Chemical Industries). Bubble liposomes were prepared from the liposomes and perfluoropropane gas (Takachiho Chemical Ind. Co. Ltd., Tokyo, Japan). In brief, 5 mL sterilized vials containing 2 mL of the liposome suspension (lipid concentration: 1 mg/mL) were filled with perfluoropropane, capped and then supercharged with 7.5 mL of perfluoropropane. The vial was placed in a bath-type sonicator (42 kHz, 100 W; BRANSONIC 2510J-DTH, Branson Ultrasonics Co., Danbury, CT) under the condition of positive pressure with perfuluoropropane in the vial under the condition of positive pressure with perfuluoropropane in the vial for 5 min to form the Bubble liposomes.

2.3. Microscopic observation of Optison and Bubble liposomes and size distribution

Optison (NEPA GENE, CO., LTD., Chiba, Japan) or Bubble liposomes were placed on glass slides, covered with a cover slip and observed with a microscope (Leica MICROSYSTEMS, Wetzlar, Germany) using a darklite illuminator (NEPA GENE). The size distribution of Optison and Bubble liposomes was measured by dynamic light scattering (ELS-800).

2.4. Transmission electron microscopy of Bubble liposomes

Bubble liposomes were suspended into sodium alginate solution (0.2% (w/v) in PBS). This suspension was dropped into calcium chloride solution (100 mM) to hold Bubble liposomes within calcium alginate gel. Then, the beads of calcium alginate gel containing Bubble liposomes were prefixed with 2% glutaraldehyde solution in 0.1 M Cacodylate buffer, post-fixed with 2% OsO_4, dehydrated with an ethanol series, and then embedded in Epan812 (polymerized at 60 °C). Ultrathin sections were made with an ultramicrotome at a thickness of 60–80 nm. Ultrathin sections were mounted on 200 mesh copper grids. They were stained with 2% uranyl acetate for 5 min and Pb for 5 min. The samples were observed with JEOL JEM12000EX at 100 kV. The treatment after prefixation was carried out in Hanaichi Ultrastructure Research Institute Co.,Ltd (Aichi, Japan).

2.5. Transfection of plasmid DNA into cells using Bubble liposomes

Luciferase cording plasmid DNA (pCMV-Luc), COS-7 cells (1×10^5 cells) and Bubble liposomes (60 μg) were suspended in culture medium (500 μL) with 10% FBS in 2 mL polypropylene tubes. The suspension was ultrasonicated using a Sonopore 4000 (6 mm diameter probe; NEPA GENE) sonicator under various conditions. The cells were washed twice with PBS, resuspended in fresh culture medium and cultured in 48-well plates for 2 days.

2.6. Transfection of plasmid DNA into cells by lipofection

Plasmid DNA (pCMV-Luc, 0.25 μg) and Lipofectin (1.25 μg) (Invitrogen) were mixed and complexed according to the manufacturer's instructions. The complex was added to COS-7 cell suspensions (1×10^5 cells/500 μL/ tube) containing various concentrations of serum for 10 s. The cells were washed twice with PBS, resuspended in fresh culture medium and cultured in 48-well plates for 2 days.

2.7. In vivo gene delivery into mouse ascites tumor cells

S-180 cells (1×10^6 cells) were *i.p.* injected into ddY mice (4 weeks old, male) (Sankyo Labo Service Corporation, Tokyo, Japan) on day 0. When S-180 cells grew as the ascites tumor in mice after 8 days of the injection [28], the mice were anaesthetized with NEMBUTAL (50 mg/kg) (Dainippon

Sumitomo Pharma, Osaka, Japan), then injected with 510 μL of pCMV-Luc (10 μg) and Bubble liposomes (500 μg) in PBS. Ultrasound (frequency: 1 MHz, duty: 50%; intensity: 1.0 W/cm^2, time: 1 min) was transdermally applied to the abdominal area using a Sonopore 3000 ultrasonicator with a probe of diameter 20mm (NEPA GENE). In other experiments, pCMV-Luc (10μg) and Lipofectin (50μg) or Lipofectamine 2000 (50μg) were mixed and complexed according to the manufacturer's instructions. The complex was suspended in PBS (510μL) and injected into the peritoneal cavities of mice. After 2days, S-180 cells were recovered from the abdomens of the mice. Then, the recovered cells were lysed in the lysis buffer (0.1M Tris–HCl (pH 7.8), 0.1% Triton X-100, 2mM EDTA) and luciferase activity was determined.

2.8. In vivo gene delivery into mouse footpad solid tumor

S-180 cells (1×10^6 cells) were inoculated into the left footpad of ddY mice (5 weeks old, male). At day 4, when the thickness of the footpad was over 3.5 mm (normal thickness was about 2 mm), the left femoral artery was exposed. One hundred μL of pCMV-Luc (10 μg) with or without Bubble liposomes (100 μg) were injected into femoral artery using 30-gauge needle. In the same time, ultrasound (frequency: 0.7 MHz, duty: 50%; intensity: 1.2 W/cm^2, time: 2 min) was transdermally applied to the tumor tissue using a Sonopore 4000 ultrasonicator with a probe of diameter 8 mm (NEPAGENE). The needle hole was then closed with an adhesive agent (Aron Alpha; Sankyo, Tokyo, Japan) and skin was put in a suture. In other samples, pCMV-Luc (10 μg) and Lipofectamine 2000 (25 μg) (Invitrogen Corporation, Carlsbad, CA) were mixed and complexed according to manual of Lipofectamine 2000. The complex were suspended in PBS (100 μL) and injected into femoral artery of mice. After 2 days of injection, the mice were sacrificed and the tumor tissues were collected. Then, the tumor tissues were homogenated in the lysis buffer and luciferase activity was determined.

2.9. Luciferase assay

Luciferase activity was measured using a luciferase assay system (Promega, Madison, WI) and a luminometer (TD-20/20, Turner Designs, Sunnyvale, CA). Activity is reported in relative light units (RLU) per mg protein.

2.10. In vivo Luciferase imaging

The mice were anaesthetized and *i.p.* injected with D-luciferin (150 mg/kg) (Xenogen, Corporation, CA). After 10 min, luciferase expression was observed with *in vivo* luciferase imaging system (IVIS) (Xenogen Corporation).

2.11. Hemolysis assay

Mouse red blood cells (2.5×10^8 cells/500 μL) were exposed with ultrasound (frequency: 0.7 MHz, Duty: 50%, Intensity: 0.5–1.5 W/cm^2, Time: 10 s.) in absent or present of Bubble liposomes. The red blood cell suspension was centrifuged for 10 min at 3000 rpm. Then, absorbance ($A_{540\ nm}$) of the supernatant was measured. The rate of hemolysis was calculated as follows: % of hemolysis = ($A_{540\ nm}$ of experimental group $-A_{540\ nm}$ of non-treated group)/($A_{540\ nm}$ of hypotonic solution treated group $-A_{540\ nm}$ of non-treated group) × 100.

2.12. In vivo studies

All experimental protocols for animal studies were in accordance with the Principle of Laboratory Animal Care in Teikyo University.

2.13. Statistical analysis

Differences in luciferase activity between experimental groups were compared with non-repeated measures ANOVA and Dunnett's test.

3. Results and discussion

The use of non-viral vectors is attractive as a safe, clinically acceptable gene therapy technique. In addition, non-viral vectors should be easy to prepare and use. However, most non-viral vectors deliver plasmid DNA into cells via endocytosis, followed by plasmid DNA degradation in the endosomes. Consequently, non-viral vectors often result in low gene delivery efficiency. It has been reported that new types of non-viral vectors can induce the escape of genes from endosomes [29–31] and directly deliver genes into the cytosol via a fusion mechanism [28,32]. In addition, microbubbles and ultrasound have been investigated with a view to improving the transfection efficiency of non-viral vectors. Gene delivery using a combination of microbubbles such as Optison and ultrasound has been widely reported. In order for extracellular plasmid DNA to be directly and effectively delivered into the cytosol, transient pores in the cell membrane must be formed by cavitation. However, conventional microbubbles are very large, with most greater than 2 μm in diameter [16]. Actually, our observations of Optison using a microscope and a darklite illuminator showed some bubbles more than 10 μm in diameter (Fig. 1(a)). In the measurement of the size distribution, there were some large microbubbles (Fig. 1d)). Tsunoda et al. pointed out that these large bubbles might cause lethal embolism in some vital organs [17]. In contrast, most Bubble liposomes were much smaller than Optison, with average diameters less than 2 μm (Fig. 1(b, e)). The injection of 1 mg of Bubble liposomes into the tail veins of mice was not lethal (data not shown), suggesting that Bubble liposomes may not cause lethal embolism. To confirm the structure of Bubble liposomes, we observed Bubble liposome with transmission electron microscopy (Fig. 1(c)). Interestingly, there were nanobubbles into lipid bilayer. From this result, it was thought that Bubble liposomes were different from conventional microbubbles which was the echo gas wrapped with lipid mono-layer. Kodama T. et al. and Klibanov A.L. et al. reported about microbubbles using distearoylphospatidylcholine and PEG-

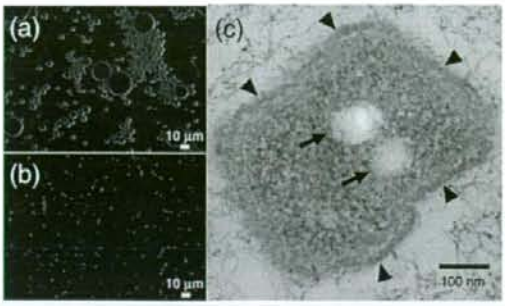

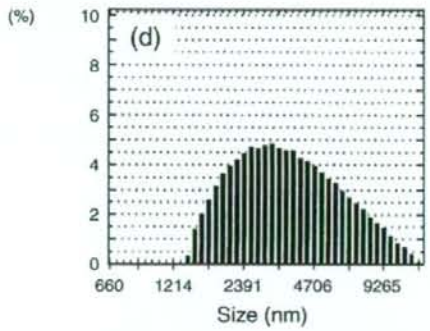

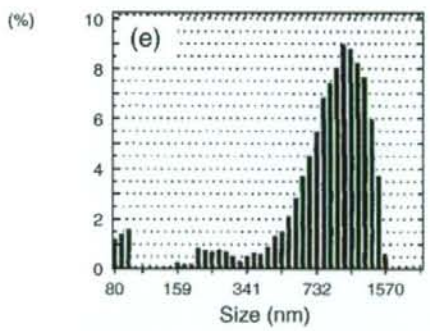

Fig. 1. Microscopy of Optison and Bubble liposomes. Optison (a) and Bubble liposomes (b) were observed with a microscope using a darklite illuminator. Original magnification ×400. Bubble liposomes (c) were observed with a transmission electric microscope at 100 kV. Original magnification ×50,000. Arrow head shows lipid bi-layer and arrow shows perfluoropropane nanobubble. The size distribution of Optison (d) and Bubble liposomes (e).

stearate [33,34]. These microbubbles were made by being stabilized hydrophobic echo gas with amphipathic molecules such as lipid and surfactant. In our method, it was thought that liposomes were reconstituted by sonication under the condition of supercharge with perfluoropropane in the 5 mL vial container. At the same time, perfluoropropane would be entrapped within lipids like micelles, which were made by DSPC and DSPE-PEG (2 k)-OMe from liposome composition, to form nanobubbles. The lipid nanobubbles were encapsulated within the reconstituted liposomes (Fig. 1(c)), which sizes were changed into around 1 μm (Fig. 1(b,e)) from 150–200 nm of original. In addition, we evaluated about the stability of Bubble liposomes by transfection efficiency with sonoporation (Fig. 2). The efficiency gradually decreased according to storage time. We also observed the aspect and ultrasound imaging of Bubble liposomes. The suspension of Bubble liposomes gradually became clear in aspects, resulted in decreasing the echo signal according to storage time (data not shown). These results suggested that perfluoropropane was gradually degassed from Bubble liposomes. Therefore, we used fresh Bubble liposomes in all experiments.

Previously, we reported that Bubble liposomes could induce cavitation and deliver plasmid DNA into various types of cells [27]. In order to examine what conditions are necessary for Bubble liposomes to efficiently deliver genes, transfection efficiency was assessed using Bubble liposomes combined with various levels of ultrasound exposure (Fig. 3(a)). COS-7 cells were exposed to various intensities of ultrasound in the presence of Bubble liposomes for 10 s. Gene transfection efficiency increased with increasing ultrasound intensity and reached a plateau at 0.7 W/cm^2. No cytotoxicity was evident even at 2.5 W/cm^2 (data not shown). The length of ultrasound exposure required to achieve gene expression was examined by measuring gene expression after 0, 1, 5 and 10 s of exposure (Fig. 3(b)). Surprisingly, gene expression was observed after 1 s of ultrasound exposure in the presence of Bubble liposomes. Transfection efficiency depended on ultrasound exposure time and reached a plateau after 5 s exposure. Efficiency was found to depend on both ultrasound intensity and exposure time (Fig. 3), indicating that Bubble liposomes can rapidly induce gene delivery while requiring only weak ultrasound, and without inducing cytotoxicity. Five seconds or 0.7 W/cm^2 of ultrasound exposure resulted in maximal gene expression, presumably due to bubble cavitation.

The transfection efficiency of some cationic non-viral vectors is significantly decreased in the presence of serum

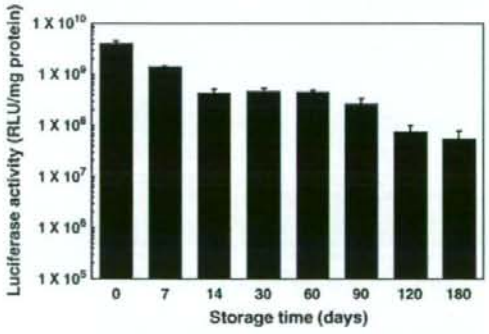

Fig. 2. Stability of Bubble liposomes. After preparation of Bubble liposomes, the vial containing Bubble liposomes was put in the refrigerator for each period. After storage, the transfection efficiency was measured with each samples. COS-7 cells (1×10^5 cells/500 μL) were mixed with pCMV-Luc (5 μg) and Bubble liposomes (60 μg). The cell mixture was exposed to ultrasound (frequency: 2 MHz, duty: 50%, burst rate: 2 Hz, intensity: 2.5 W/cm^2, time: 10 s.). The cells were washed and cultured for 2 days, then luciferase activity was determined as described in Materials and methods. Each bar represents the mean±S.D. for triplicate.

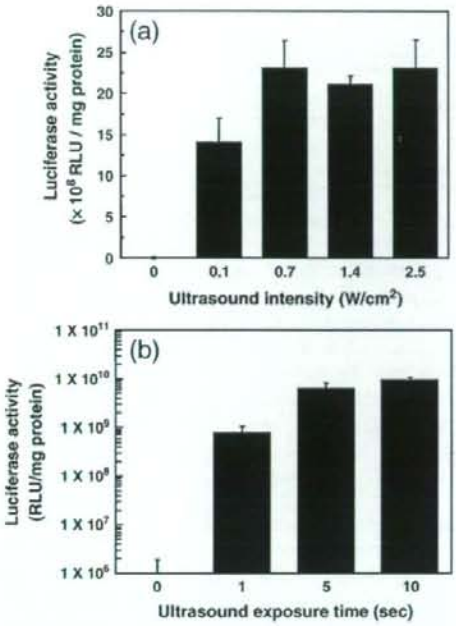

Fig. 3. Effect of ultrasound conditions on transfection efficiency with Bubble liposomes. COS-7 cells (1×10^5 cells/500 μL) were mixed with pCMV-Luc (5 μg) and Bubble liposomes (60 μg). The cell mixture was exposed to ultrasound (a): (frequency: 2 MHz, duty: 50%, burst rate: 2 Hz, intensity: 0–2.5 W/cm^2, time: 10 s.) or (b): (frequency: 2 MHz, duty: 50%, burst rate: 2 Hz, intensity: 2.5 W/cm^2, time: 0–10 s.). The cells were washed and cultured for 2 days, then luciferase activity was determined as described in Materials and methods. Each bar represents the mean±S.D. for triplicate.

due to an interaction between serum proteins and the cationic vectors [28]. Whereas, transfection efficiency with the combination of Bubble liposomes and ultrasound did not decrease even in the presence of 50% serum in *in vitro* study [27]. In the next examination, we examined whether Bubble liposomes could deliver plasmid DNA into S-180 ascites tumor cells in living animals after local injection (Fig. 4). In this examination, we compared the transfection efficiency with Bubble liposomes or cationic liposomes such as Lipofectin and Lipofectamine 2000. Luciferase expression was low in the mice treated with lipofectin-plasmid DNA complexes prepared by the traditional lipofection method, presumably because the complexes were associated with various proteins in the peritoneal cavity. On the other hand, luciferase expression increased in the mice treated with Lipofectamine 2000-plasmid DNA complexes compare with Lipofectin, because it was known that LF2000 was better than Lipofectin for gene delivery in the presence of serum. In addition, luciferase expression in mice treated with plasmid DNA, Bubble liposomes and ultrasound exposure was higher than that in the mice treated with Lipofectamine 2000-plasmid DNA complexes. This result supported the previous our report. In short, it was thought that Bubble liposomes and ultrasound was not affected by proteins existing in the peritoneal cavity and this method immediately and directly delivered plasmid DNA into cells with the mechanism which was not endocytosis pathway in lipofection method. We also confirmed that ultrasound combined with Bubble liposomes was effective at delivering genes to other tissues in the peritoneal cavity such as stomach, kidney, liver, spleen, intestine, diaphragm, pancreas, peritoneum and mesentery. Luciferase activity in these tissues was much lower than that observed in the S-180 cells (less than 130 RLU/mg protein).

Mizuguchi et al. reported about the effective cancer gene therapy by cytokine provision in the local area via gene delivery into arteries leading to tumor or arteries in tumor tissue [35]. Previously, we succeeded the gene delivery into artery of ultrasound exposure site with Bubble liposomes [27]. Therefore, we thought that our technology could be applied to establish the tumor tissue specific gene delivery. In this time, we attempted to deliver plasmid DNA to solid tumor via the injection into the artery that lead to tumor (Fig. 5). In Fig. 4, Lipofectin did not work well as gene delivery tool. In this study, we only used Lipofectamine 2000 as a control. In the mice treated with plasmid DNA and ultrasound, luciferase expression was same low level in the mice of plasmid DNA injection. And, luciferase expression was also low level in the mice treated with Lipofectamine 2000 and plasmid DNA complex, although the complex could be induced into S-180 ascites tumor cells. Generally, enough time is necessary for the complex to bind to cell surface and deliver plasmid DNA into cells. In this case, there was no time for the complex to retain in tumor tissue after injection because of blood stream and it would be resulted in

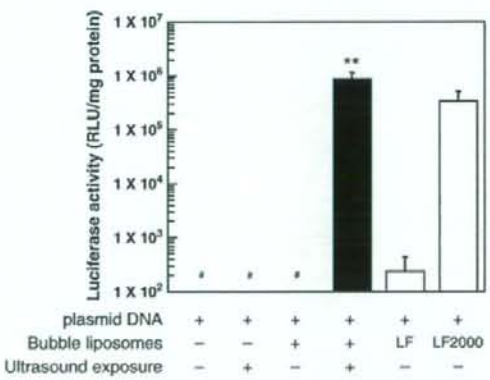

Fig. 4. *In vivo* gene delivery into mouse ascites tumor cells with Bubble liposomes. S-180 cells (1×10^6 cells) were i.p. injected into ddY mice. After 8 days, the mice were anaesthetized, then injected with 510 μL of pCMV-Luc (10 μg) and Bubble liposomes (500 μg) in PBS. Ultrasound (frequency: 1 MHz, duty: 50%; intensity: 1.0 W/cm^2, time: 1 min) was transdermally applied to the abdominal area. In another experiment, pCMV-Luc (10 μg) — Lipofectin (50 μg) or Lipofectamine 2000 (50 μg) complex was suspended in PBS (510 μL) and injected into the peritoneal cavity of mice. After 2 days, S-180 cells were recovered from the abdomens of the mice. Luciferase activity was determined as described in Materials and methods. Each bar represents the mean±S.D. for three to six mice/group. $^{**}P<0.01$ compared to the group treated with plasmid DNA, Bubble liposomes, ultrasound exposure or lipofection with Lipofectin or Lipofectamine 2000. LF, Lipofectin. LF2000, Lipofectamine 2000. #<10^2 RLU/mg protein.

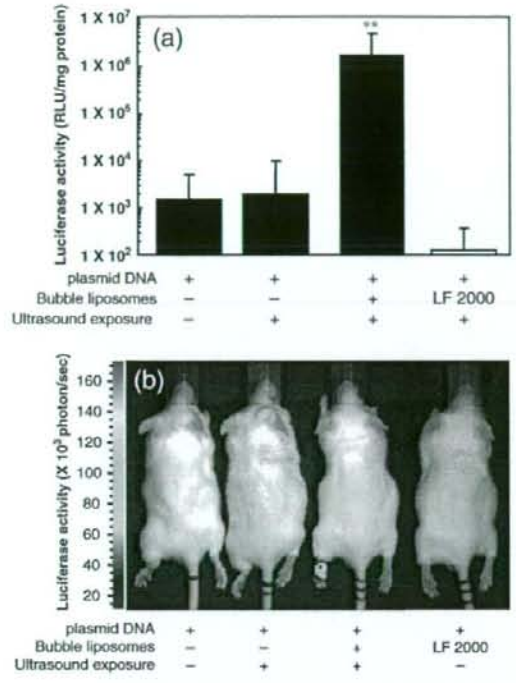

Fig. 5. *In vivo* gene delivery into mouse solid tumor with Bubble liposomes. S-180 cells (1×10^6 cells) were inoculated into left footpad of ddY mice. After 4 days, the mice were anaesthetized, then injected with 100 mL of pCMV-Luc (10 μg) in absent or present of Bubble liposomes (100 μg) in PBS. Ultrasound (frequency: 0.7 MHz, duty: 50%; intensity: 1.2 W/cm^2, time: 1 min) was transdermally exposed to tumor tissue. In another experiment, pCMV-Luc (10 μg) — Lipofectamine 2000 (25 μg) complex was suspended in PBS (100 μL) and injected into the left femoral artery. After 2 days, tumor tissue was recovered the mice. Luciferase activity was determined as described in Materials and methods. (a) Luciferase activity in solid tumor. Each bar represents the mean±S.D. for five mice/group. $^{**}P<0.01$ compared to the group treated with plasmid DNA, ultrasound exposure or Lipofectamine 2000. (b) *In vivo* luciferase imaging in the solid tumor bearing mice. The photon counts are indicated by the pseudo-color scales. LF 2000, Lipofectamine 2000.

low efficiency of transfection. On the other hand, luciferase expression in the combination of Bubble liposomes and ultrasound was much higher than that in other group (Fig. 5(a)). Koch et al. reported that the combination of ultrasound and microbubble (Levovist) enhanced lipoplex-mediated cell transfection efficiency *in vitro* and also severely damaged most cells. [36]. Therefore, we attempted to confirm the enhancement of transcfection efficiency with Lipofectamine 2000 by Bubble liposomes and ultrasound in the condition without cell damage. The transfection efficiency with lipoplex was not enhanced with Bubble liposomes and ultrasound *in vitro* and *in vivo* (data not shown). The size of Lipofectamine 2000-plasmid DNA complexes was larger than that of naked plasmid DNA by forming the spaghetti–meatball like structure. We guessed that it was difficult for the complexes to enter into cytosol via transient pore on the membrane with cavitation of Bubble liposomes in the condition without cell damage. In the Koch's report, ultrasound was exposed to *in vitro* cells for 60 s with Levovist (20 and 200 mg/mL). In this study, Bubble liposomes (1 mg/mL) were injected into the femoral artery. The concentration of Bubble liposomes would be much lower than that of Levovist because of the dilution of Bubble liposomes in the blood. In addition, the time of ultrasound exposure to Bubble liposomes was very short because of blood flow. Therefore, I thought that the transfection efficiency in the combination of cavitation with Bubble liposomes and lipoplexes was not enhanced. To evaluate gene expression site, we observed luciferase expression with luciferase *in vivo* imaging system (Fig. 5(b)). In the mice treated with Bubble liposomes and ultrasound, luciferase expression was observed in the tumor tissue because of inducing cavitation at ultrasound exposure site. Then, there were a possibility of hemolysis by the cavitation of Bubble liposomes in artery. We examined about hemolytic effect in the treatment of Bubble liposomes and ultrasound (Fig. 6). When the ultrasound was exposed to red blood cell with or without Bubble liposomes *in vitro*, serious hemolysis was not induced. These results suggested that this gene delivery system was important method to achieve tumor specific gene delivery without serious damage.

Plasmid DNA was effectively delivered into S-180 ascites tumor cells and solid tumor tissues with Bubble liposomes and ultrasound, although plasmid DNA did not form a complex with Bubble liposomes because Bubble liposomes were made of neutral charge lipids and modified polyethylene glycol on the surface, and existed free *in vivo*. These results could be explained from Fig. 3. In short, it is thought that Bubble liposomes can immediately and effectively deliver plasmid DNA into cells *in vivo* before the plasmid DNA is degraded by DNase. A mixture of plasmid DNA and Bubble liposomes was injected into mice, and the plasmid DNA was delivered to a specific area of the abdomen or solid tumor tissue by local exposure to ultrasound, suggesting that gene targeting can be induced at a site by exposure to ultrasound. In future studies, we intend to establish minimally-invasive and tissue-specific gene delivery with Bubble liposomes after systemic injection.

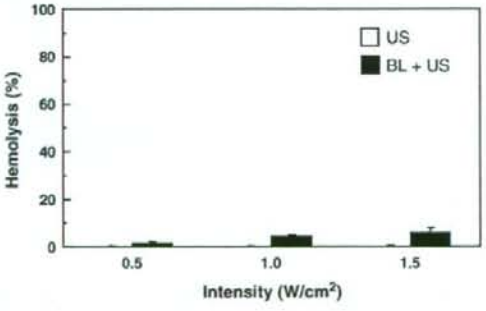

Fig. 6. Hemolysis of red blood cells by Bubble liposomes and ultrasound. Mouse red blood cells (2.5×10^8 cells/ 500 mL) were exposed with ultrasound (frequency: 0.7 MHz, Duty: 50%, Intensity: 0.5–1.5 W/cm^2, Time: 10 s.) in absent or present of Bubble liposomes. Hemolysis was assessed as described in Materials and methods. Each bar represents the mean±S.D. for triplicate.

The present study showed that Bubble liposomes can be a more effective gene delivery tools into tumor *in vivo* than conventional lipofection. Moreover, Bubble liposomes are an attractive gene delivery approach in cancer gene therapy as the method is minimally-invasive and tumor specific gene transfer, requiring only exposure to ultrasound applied to the surface of the body.

Acknowledgements

We are grateful to Dr. Katsuro Tachibana (Department of Anatomy, School of Medicine, Fukuoka University) for technical advice regarding the induction of cavitation with ultrasound, to Mr. Katsutoshi Kurosawa, Mr. Takamichi Todoroki, Ms. Hitomi Tamagawa (Department of Biopharmaceutics, School of Pharmaceutical Sciences, Teikyo University) for excellent technical assistance, to Dr. Akinori Suginaka (NOF CORPORATION) for technical advice regarding lipids and for providing the lipids, and to Mr. Yasuhiko Hayakawa, Mr. Takahiro Yamauchi and Mr. Kosho Suzuki (NEPA GENE CO., LTD.) for technical advice regarding ultrasound exposure.

This study was supported by an Industrial Technology Research Grant (04A05010) in 2004 from the New Energy and Industrial Technology Development Organization (NEDO) of Japan, a Grant-in-Aid for Young Scientists (160700392, 19700423), Exploratory Research (16650126) from the Japan Society for the Promotion of Science and a Research on Advanced Medical Technology (17070301) in Health and Labour Sciences Research Grants from Ministry of Health, Labour and Welfare.

References

[1] M. Fechheimer, J.F. Boylan, S. Parker, J.E. Sisken, G.L. Patel, S.G. Zimmer, Transfection of mammalian cells with plasmid DNA by scrape loading and sonication loading, Proc. Natl. Acad. Sci. U. S. A. 84 (1987) 8463–8467.

[2] M.W. Miller, D.L. Miller, A.A. Brayman, A review of in vitro bioeffects of inertial ultrasonic cavitation from a mechanistic perspective, Ultrasound Med. Biol. 22 (1996) 1131–1154.

[3] M. Joersbo, J. Brunstedt, Protein synthesis stimulated in sonicated sugar beet cells and protoplasts, Ultrasound Med. Biol. 16 (1990) 719–724.

[4] H.R. Guzman, A.J. McNamara, D.X. Nguyen, M.R. Prausnitz, Bioeffects caused by changes in acoustic cavitation bubble density and cell concentration: a unified explanation based on cell-to-bubble ratio and blast radius, Ultrasound Med. Biol. 29 (2003) 1211–1222.

[5] D.L. Miller, S.V. Pislaru, J.E. Greenleaf, Sonoporation: mechanical DNA delivery by ultrasonic cavitation, Somat. Cell Mol. Genet. 27 (2002) 115–134.

[6] W. Wei, B. Zheng-zhong, W. Yong-jie, Z. Qing-wu, M. Ya-lin, Bioeffects of low-frequency ultrasonic gene delivery and safety on cell membrane permeability control, J. Ultrasound. Med. 23 (2004) 1569–1582.

[7] M. Duvshani-Eshet, M. Machluf, Therapeutic ultrasound optimization for gene delivery: a key factor achieving nuclear DNA localization, J. Control Release 108 (2005) 513–528.

[8] H.J. Kim, J.F. Greenleaf, R.R. Kinnick, J.T. Bronk, M.E. Bolander, Ultrasound-mediated transfection of mammalian cells, Hum. Gene Ther. 7 (1996) 1339–1346.

[9] D.B. Tata, F. Dunn, D.J. Tindall, Selective clinical ultrasound signals mediate differential gene transfer and expression in two human prostate cancer cell lines: LnCap and PC-3, Biochem. Biophys. Res. Commun. 234 (1997) 64–67.

[10] W.J. Greenleaf, M.E. Bolander, G. Sarkar, M.B. Goldring, J.F. Greenleaf, Artificial cavitation nuclei significantly enhance acoustically induced cell transfection, Ultrasound Med. Biol. 24 (1998) 587–595.

[11] T. Li, K. Tachibana, M. Kuroki, M. Kuroki, Gene transfer with echo-enhanced contrast agents: comparison between Albunex, Optison, and Levovist in mice-initial results, Radiology 229 (2003) 423–428.

[12] R.V. Shohet, S. Chen, Y.T. Zhou, Z. Wang, R.S. Meidell, R.H. Unger, P.A. Grayburn, Echocardiographic destruction of albumin microbubbles directs gene delivery to the myocardium, Circulation 101 (2000) 2554–2556.

[13] S. Sonoda, K. Tachibana, E. Uchino, A. Okubo, M. Yamamoto, K. Sakoda, T. Hisatomi, K.H. Sonoda, Y. Negishi, Y. Izumi, S. Takao, T. Sakamoto, Gene transfer to corneal epithelium and keratocytes mediated by ultrasound with microbubbles, Investig. Ophthalmol. Vis. Sci. 47 (2006) 558–564.

[14] Y. Taniyama, K. Tachibana, K. Hiraoka, M. Aoki, S. Yamamoto, K. Matsumoto, T. Nakamura, T. Ogihara, Y. Kaneda, R. Morishita, Development of safe and efficient novel nonviral gene transfer using ultrasound: enhancement of transfection efficiency of naked plasmid DNA in skeletal muscle, Gene Ther. 9 (2002) 372–380.

[15] Y. Taniyama, K. Tachibana, K. Hiraoka, T. Namba, K. Yamasaki, N. Hashiya, M. Aoki, T. Ogihara, K. Yasufumi, R. Morishita, Local delivery of plasmid DNA into rat carotid artery using ultrasound, Circulation 105 (2002) 1233–1239.

[16] J.R. Lindner, Microbubbles in medical imaging: current applications and future directions, Nat. Rev. Drug Discov. 3 (2004) 527–532.

[17] S. Tsunoda, O. Mazda, Y. Oda, Y. Iida, S. Akabame, T. Kishida, M. Shin-Ya, H. Asada, S. Gojo, J. Imanishi, H. Matsubara, T. Yoshikawa, Sonoporation using microbubble BR14 promotes pDNA/siRNA transduction to murine heart, Biochem. Biophys. Res. Commun. 336 (2005) 118–127.

[18] M. Harata, Y. Soda, K. Tani, J. Ooi, T. Takizawa, M. Chen, Y. Bai, K. Izawa, S. Kobayashi, A. Tomonari, F. Nagamura, S. Takahashi, K. Uchimaru, T. Iseki, T. Tsuji, T.A. Takahashi, K. Sugita, S. Nakazawa, A. Tojo, K. Maruyama, S. Asano, CD19-targeting liposomes containing imatinib efficiently kill Philadelphia chromosome-positive acute lymphoblastic leukemia cells, Blood 104 (2004) 1442–1449.

[19] O. Ishida, K. Maruyama, H. Tanahashi, M. Iwatsuru, K. Sasaki, M. Eriguchi, H. Yanagie, Liposomes bearing polyethyleneglycol-coupled transferrin with intracellular targeting property to the solid tumors in vivo, Pharm. Res. 18 (2001) 1042–1048.

[20] K. Kawamura, N. Kadowaki, R. Suzuki, S. Udagawa, S. Kasaoka, N. Utoguchi, T. Kitawaki, N. Sugimoto, N. Okada, K. Maruyama, T. Uchiyama, Dendritic cells that endocytosed antigen-containing IgG-liposomes elicit effective antitumor immunity, J. Immunother. 29 (2006) 165–174.

[21] K. Maruyama, E. Holmberg, S.J. Kennel, A. Klibanov, V.P. Torchilin, L. Huang, Characterization of in vivo immunoliposome targeting to pulmonary endothelium, J. Pharm. Sci. 79 (1990) 978–984.

[22] K. Maruyama, O. Ishida, S. Kasaoka, T. Takizawa, N. Utoguchi, A. Shinohara, M. Chiba, H. Kobayashi, M. Eriguchi, H. Yanagie, Intracellular targeting of sodium mercaptoundecahydrododecaborate (BSH) to solid tumors by transferrin-PEG liposomes, for boron neutron-capture therapy (BNCT), J. Control. Release 98 (2004) 195–207.

[23] K. Maruyama, S.J. Kennel, L. Huang, Lipid composition is important for highly efficient target binding and retention of immunoliposomes, Proc. Natl. Acad. Sci. U. S. A. 87 (1990) 5744–5748.

[24] H. Yanagie, K. Maruyama, T. Takizawa, O. Ishida, K. Ogura, T. Matsumoto, Y. Sakurai, T. Kobayashi, A. Shinohara, J. Rant, J. Skvarc, R. Ilic, G. Kuhne, M. Chiba, Y. Furuya, H. Sugiyama, T. Hisa, K. Ono, H. Kobayashi, M. Eriguchi, Application of boron-entrapped stealth liposomes to inhibition of growth of tumour cells in the in vivo boron neutron-capture therapy model, Biomed. Pharmacother. 60 (2006) 43–50.

[25] H. Yanagie, K. Ogura, K. Takagi, K. Maruyama, T. Matsumoto, Y. Sakurai, J. Skvarc, R. Illic, G. Kuhne, T. Hisa, I. Yoshizaki, K. Kono, Y. Furuya, H. Sugiyama, H. Kobayashi, K. Ono, K. Nakagawa, M. Eriguchi, Accumulation of boron compounds to tumor with polyethylene-glycol binding liposome by using neutron capture autoradiography, Appl. Radiat. Isotopes 61 (2004) 639–646.

[26] H. Hatakeyama, H. Akita, K. Kogure, M. Oishi, Y. Nagasaki, Y. Kihira, M. Ueno, H. Kobayashi, H. Kikuchi, H. Harashima, Development of a novel

systemic gene delivery system for cancer therapy with a tumor-specific cleavable PEG-lipid, Gene Ther. 14 (2007) 68–77.
[27] R. Suzuki, T. Takizawa, Y. Negishi, K. Hagisawa, K. Tanaka, K. Sawamura, N. Utoguchi, T. Nishioka, K. Maruyama, Gene delivery by combination of novel liposomal bubbles with perfluoropropane and ultrasound, J. Control. Release 117 (2007) 130–136.
[28] H. Mizuguchi, T. Nakagawa, M. Nakanishi, S. Imazu, S. Nakagawa, T. Mayumi, Efficient gene transfer into mammalian cells using fusogenic liposome, Biochem. Biophys. Res. Commun. 218 (1996) 402–407.
[29] K. Kono, Y. Torikoshi, M. Mitsutomi, T. Itoh, N. Emi, H. Yanagie, T. Takagishi, Novel gene delivery systems: complexes of fusigenic polymer-modified liposomes and lipoplexes, Gene Ther. 8 (2001) 5–12.
[30] N. Sakaguchi, C. Kojima, A. Harada, K. Koiwai, K. Shimizu, N. Emi, K. Kono, Enhancement of transfection activity of lipoplexes by complexation with transferrin-bearing fusogenic polymer-modified liposomes, Int. J. Pharm. 325 (2006) 186–190.
[31] T. Kakudo, S. Chaki, S. Futaki, I. Nakase, K. Akaji, T. Kawakami, K. Maruyama, H. Kamiya, H. Harashima, Transferrin-modified liposomes equipped with a pH-sensitive fusogenic peptide: an artificial viral-like delivery system, Biochemistry 43 (2004) 5618–5628.
[32] M. Kondoh, T. Matsuyama, R. Suzuki, H. Mizuguchi, T. Nakanishi, S. Nakagawa, Y. Tsutsumi, M. Nakanishi, M. Sato, T. Mayumi, Growth inhibition of human leukemia HL-60 cells by an antisense phosphodiester oligonucleotide encapsulated into fusogenic liposomes, Biol. Pharm. Bull. 23 (2000) 1011–1013.
[33] H. Leong-Poi, J. Christiansen, A.L. Klibanov, S. Kaul, J.R. Lindner, Noninvasive assessment of angiogenesis by ultrasound and microbubbles targeted to alpha(v)-integrins, Circulation 107 (2003) 455–460.
[34] M. Takahashi, K. Kido, A. Aoi, H. Furukawa, M. Ono, T. Kodama, Spinal gene transfer using ultrasound and microbubbles, J. Control. Release 117 (2007) 267–272.
[35] H. Mizuguchi, T. Nakagawa, S. Toyosawa, M. Nakanishi, S. Imazu, T. Nakanishi, Y. Tsutsumi, S. Nakagawa, T. Hayakawa, N. Ijuhin, T. Mayumi, Tumor necrosis factor alpha-mediated tumor regression by the in vivo transfer of genes into the artery that leads to tumors, Cancer Res. 58 (1998) 5725–5730.
[36] S. Koch, P. Pohl, U. Cobet, N.G. Rainov, Ultrasound enhancement of liposome-mediated cell transfection is caused by cavitation effects, Ultrasound Med. Biol. 26 (2000) 897–903.

The American Journal of Pathology, Vol. 173, No. 6, December 2008

DOI: 10.2353/ajpath.2008.080684

Neurobiology

Loss of Hrs in the Central Nervous System Causes Accumulation of Ubiquitinated Proteins and Neurodegeneration

Keiichi Tamai,*† Masafumi Toyoshima,‡ Nobuyuki Tanaka,*§†† Noriko Yamamoto,‖ Yuji Owada,‖ Hiroshi Kiyonari,** Kazuko Murata,* Yoshiyuki Ueno,† Masao Ono,¶ Tooru Shimosegawa,† Nobuo Yaegashi,‡ Masahiko Watanabe,‡‡ and Kazuo Sugamura*

From the Departments of Microbiology and Immunology, Gastroenterology,† Obstetrics and Gynecology,‡ Cancer Science,§ and Pathology,¶ Tohoku University Graduate School of Medicine, Sendai; the Department of Organ Anatomy,‖ Yamaguchi University Graduate School of Medicine, Yamaguchi; the Laboratory for Animal Resources and Genetic Engineering,** Center for Developmental Biology, Riken Kobe, Kobe; the Division of Immunology,†† Miyagi Cancer Center Research Institute, Natori; and the Department of Anatomy,‡‡ Hokkaido University School of Medicine, Sapporo, Japan*

The endosomal sorting complex required for transport (ESCRT) proteins form multimolecular complexes that control multivesicular body formation, endosomal sorting, and transport ubiquitinated membrane proteins (including cell-surface receptors) to the endosomes for degradation. There is accumulating evidence that endosomal dysfunction is linked to neural cell degeneration *in vitro*, but little is known about the relationship between neural disorders and ESCRT proteins *in vivo*. Here we specifically deleted the *hrs* gene, ESCRT-0, in the neurons of mice by crossing *loxP*-flanked *hrs* mice with transgenic mice expressing the synapsin-I Cre protein (*SynI-cre*). Histological analyses revealed that both apoptosis and a loss of hippocampal CA3 pyramidal neurons occurred in the $hrs^{flox/flox}$;*SynI-cre* mice. Notably, the $hrs^{flox/flox}$;*SynI-cre* mice accumulated ubiquitinated proteins, such as glutamate receptors and an autophagy-regulating protein, p62. These molecules are particularly prominent in the hippocampal CA3 neurons and cerebral cortex with advancing age. Accordingly, we found that both locomotor activity and learning ability were severely reduced in the $hrs^{flox/flox}$;*SynI-cre* mice. These data suggest that Hrs plays an important role in neural cell survival *in vivo* and provide an animal model for neurodegenerative diseases that are known to be commonly affected by the generation of proteinaceous aggregates. *(Am J Pathol 2008, 173:1806–1817; DOI: 10.2353/ajpath.2008.080684)*

The generation of proteinaceous aggregates is a common pathological feature in neurodegenerative diseases.[1] Alterations in the lysosomal pathway are associated with normal brain aging, as well as with age-related neurodegenerative diseases, including Alzheimer's and Parkinson's. When the level of misfolded protein overwhelms the degradative pathways, cellular toxicity and neurodegeneration result.[2] Cellular mechanisms for degrading misfolded protein include the ubiquitin-proteasome system, which is the main nonlysosomal degradative pathway for ubiquitinated proteins, and autophagy, a lysosome-mediated degradative pathway.[3]

Glutamate receptors play prominent roles in several neurodegenerative diseases.[4–7] All *N*-methyl-D-aspartate (NMDA) receptors (NR) share one NR1 subunit and one or more NR2A-D and/or NR3 subunits, forming a heterotetrameric complex.[8] Fbx2-mediated ubiquitination is required for NR1 subunit degradation.[9] KEL-8, a substrate receptor for Cullin 3 ubiquitin ligases, is reported to be required for the proteolysis of the α-amino-3-hydroxy-5-methyl-isoxazolepropionic acid receptor (AMPAR) subunit GluR1.[10] Thus, ubiquitination is important for the homeostatic control of glutamate receptors in neurons.

Supported in part by the Ministry of Education, Culture, Sports, Science, and Technology of Japan (grants-in-aid for Scientific Research on Priority Areas 19041067 and 20012053 to N.T. and 19059001 to K.S.); the Japan Society for the Promotion of Science [grants-in-aid for Scientific Research (C) 19590484 to N.T. and 19590488 to K.M. and a grant-in-aid for Exploratory Research 19659108 to K.S.]; and the Naito Research Foundation.

Accepted for publication September 4, 2008.

Address reprint requests to Nobuyuki Tanaka, Department of Microbiology and Immunology, Tohoku University Graduate School of Medicine, 2-1 Seiryo-machi, Aoba-ku, Sendai, 980-8575 Japan. E-mail: n-tanaka@m.tains.tohoku.ac.jp.

Endosomal sorting complex required for transport (ESCRT) proteins form multimolecular complexes that control multivesicular body formation and transport ubiquitinated membrane proteins to the endosomes. The ESCRTs are subdivided into four complexes.[11] Ubiquitinated cargos such as epidermal growth factor receptors are initially recognized by the ESCRT-0 complex, and then sequentially handed off to ESCRT-I, -II, and -III. After these steps, the cargos are invaginated into multivesicular bodies and eventually sorted into the lysosomes. The ESCRT-0 component Hrs (also known as Hgs) plays a particularly major role in this sorting process.[12] Although several studies using Hrs mutants or its deletion in mammalian cells and mice suggest that it has a role in morphogenesis and development,[13,14] whether or not Hrs possesses any function in the nervous system is unknown.

Recent studies suggest that protein ubiquitination is essential for proper nervous system function.[15] Ubiquitination is a key tagging process for proper protein trafficking and turnover involving proteasome- and lysosome-dependent degradation. In addition, a recent study suggested that normal multivesicular body function is essential for neural cells to avoid degeneration.[16] Furthermore, ESCRT-III dysfunction is associated with a type of neurodegeneration that resembles frontotemporal dementia and other age-dependent neurodegenerative diseases.[17] These findings together highlight ESCRT function as being important for maintaining neuronal homeostasis, and prompted us to investigate the *in vivo* role of Hrs in the central nervous system. Using the Cre-loxP system, we found that Hrs is required for the degradation of ubiquitinated proteins in the central nervous system and the survival of mouse hippocampal CA3 neurons.

Materials and Methods

Generation of Floxed Hrs Mice

To generate a neuron-specific conditional knockout of Hrs (accession no. CDB0476K; Center for Developmental Biology, Kobe, Japan), we generated a floxed *hrs* allele (hrs^{flox}) using embryonic stem (ES) cell homologous recombination technology. For the targeting construct of the $hrs^{flox/flox}$ line, a C57BL/6J genomic clone was used to generate the *hrs* targeting vector, and two *loxP* sites were integrated, one upstream of exon 2 and one downstream of exon 4. The targeting vector was electroporated into TT2 ES cells, followed by G418 selection. Colonies surviving selection were tested for homologous recombination and incorporation of the *loxP* sites by Southern blot hybridization. Two clones were identified and injected into ICR 8 cell-stage embryos.[18] Chimeric mice were mated to C57BL/6J mice to identify germ-line transmission of the targeted *hrs* allele. Removal of the neomycin selection cassette, which was surrounded by *FRT* (Flp recombinase target) sites, was accomplished by first mating $hrs^{flox/flox}$ mice to FLPeR mice[19] at Riken (Kobe, Japan). All animal experiments were performed according to the guidelines laid down by the animal welfare committees of the Tohoku University Graduate School of Medicine and Riken.

Generation of $hrs^{flox/flox}$;Synl-cre Mice

Synl-cre transgenic mice (a gift from Jamey Marth, University of California, San Diego, CA)[20] were mated with the $hrs^{flox/flox}$ mice to generate $hrs^{flox/+}$;*Synl-cre* mice. The $hrs^{flox/+}$;*Synl-cre* mice were then mated with each other. Offspring carrying $hrs^{flox/flox}$;*Synl-cre* and $hrs^{+/+}$;*Synl-cre* were used for further analyses. These mice were genotyped by polymerase chain reaction (PCR) using DNA obtained from the tail.

Southern Blot Analysis

Genomic DNA from ES cells was digested with restriction enzymes, separated by electrophoresis on a 0.6% agarose gel, transferred to Hybond-N (GE Health Care, Chalfont St. Giles, UK, and hybridized with the random-primed probe.

Genotype Analysis

Genomic DNA from the mouse tail was used for PCR analysis. We genotyped the *hrs* flox allele using a forward primer (5′-GATGATGAGATGTTTACC-3′) and a reverse primer (5′-TTGTCCTTTACCTCTTAG-3′) that flank the 5′ *loxP* site. The PCR products were 354 bp for the $hrs^{flox/flox}$ allele and 229 bp for the wild-type allele. We amplified the $hrs^{\Delta 2-4}$ allele using a forward (6851F: 5′-TTGTTGAATGAGTAACAAGGGTGGT-3′) and reverse primer (9100R: 5′-TGGATCCCATGAAATGGGGAACAGC-3′). The PCR products were 0.3 kbp for the $hrs^{\Delta 2-4}$ allele and 2.3 kbp for the wild-type allele. Genotyping for the presence of the *Synl-cre* allele was performed using the following primer pair: forward (5′-TTACCGGTCGATGCAACGAGTGAT-3′) and reverse (5′-TTCCATGAGTGAACGAACCTGGTC-3′).

Western Blotting

Immunoblotting was performed as previously described.[21] In brief, brains from mice were homogenized in lysis buffer [1% Nonidet P-40, 20 mmol/L Tris-HCl (pH 7.5), 150 mmol/L NaCl, 1 mmol/L ethylenediaminetetraacetic acid, 1 mmol/L Na_3VO_4, 1 mmol/L phenylmethyl sulfonyl fluoride, and 20 μg/ml aprotinin]. The lysates were precleared by centrifugation (10,000 × *g*) for 20 minutes at 4°C. The supernatants were then separated by sodium dodecyl sulfate-polyacrylamide gel electrophoresis and transferred onto polyvinylidene difluoride membranes (Millipore, Billerica, MA). After being blocked with 5% nonfat milk in Tris-buffered saline containing 0.1% Tween 20, the membranes were probed with the indicated primary antibodies. After another wash, the membranes were probed with horseradish peroxidase-conjugated secondary antibodies (Cell Signaling, Beverly, MA).

Histology and Immunohistochemistry

Mice were perfused with 4% paraformaldehyde, and the dissected brains were postfixed for 24 hours before being embedded in paraffin. For histological analyses, 3-μm sections were stained with hematoxylin and eosin (H&E). Immunostaining was performed by the streptavidin-biotin immunoperoxidase method (Histofine SAB-PO kit; Nichirei, Tokyo, Japan) using primary antibodies. We used the antibodies at the following dilutions: anti-ubiquitin [1:200, 1B3, mouse monoclonal antibody (mAb); MBL International, Woburn, MA]; anti-ubiquitin (1:200, FK2, mAb; Biomol, Plymouth Meeting, PA); anti-GFAP (1:200, mouse mAb; Chemicon, Temecula, CA); anti-calbindin (1:200, rabbit polyclonal antibody; Chemicon). We also used anti-Hrs,[22] anti-NR1,[23] anti-NR2B,[24] and anti-GluR1 antibodies[25] as previously described. To detect mouse monoclonal antibodies, the Histofine mouse staining kit (Nichirei) was used. Immunoreactions were visualized with 3,3,-diaminobenzidine. For terminal deoxynucleotidyltransferase-mediated dUTP-biotin nick-end labeling (TUNEL) assays, 5-μm sections were deparaffinized, and terminal transferase labeling of the fragmented DNA was performed with an *in situ* cell death detection kit (Fluorescein; Roche, Indianapolis, IN), according to the assay protocol of the kit.

Reverse Transcriptase (RT)-PCR

RT-PCR was performed as previously described.[26] In brief, the total RNA from the brains of 8-week-old *hrs*$^{+/+}$; *Synl-cre* and *hrs*$^{flox/flox}$;*Synl-cre* mice was prepared using TRIzol (Invitrogen, Carlsbad, CA). PCR was performed in a 50-μl mixture consisting of 20 mmol/L Tris-HCl (pH 8.0), 2 mmol/L $MgCl_2$,50 mmol/L KCl, 0.2 mmol/L deoxynucleotide triphosphate mixture, 1 μmol/L of various primers, 1.25 U of Ex-TaqDNA polymerase (Takara Shuzo, Kyoto, Japan), and 1 μl of the RT reaction mixture as a template. The PCR conditions were as follows: denaturation at 94°C for 2 minutes, followed by 35 cycles of 30 seconds at 94°C, 1 minute at 65°C, and 1 minute at 72°C. The following oligonucleotide primers were used: HrsE1F (5′-GAGGCAGCGGCACCTTCGAG-3′) and HrsE7R (5′-ATGGCATTCCTCAGCATCCA-3′).

In Situ *Hybridization*

In situ hybridization was performed as previously described.[27] Mice were anesthetized and perfused with 4% paraformaldehyde. The brains were postfixed overnight at 4°C and then cryoprotected with 30% sucrose in 0.1 M phosphate buffer at 4°C. Frozen sections were cut at 20 μm on a freezing microtome and mounted on MAS-coated slides (Matsunami, Osaka, Japan). The transcription reactions were performed using a digoxigenin (DIG) RNA labeling kit (SP6/T7) (Roche). The purified plasmids were linearized and then used as templates for *in vitro* transcription of the DIG-labeled antisense (or sense control) RNA probes with T7 (or SP6) RNA polymerase. The transcripts were subjected to alkaline hydrolysis to reduce their size. For this, the DIG-labeled full-length cRNA was added to alkaline hydrolysis solution [40 mmol/L $NaHCO_3$/60 mmol/L Na_2CO_3 (pH 10.2)] and incubated for 15 minutes at 60°C. For *in situ* hybridization, the sections were postfixed in 4% paraformaldehyde [freshly prepared in 0.1 mol/L phosphate buffer (pH 7.4)] for 10 minutes, washed three times with phosphate-buffered saline (PBS), treated with 0.5 μg/ml proteinase K (Sigma) for 30 minutes at 37°C, postfixed in 4% paraformaldehyde for 5 minutes, washed three times with PBS, acetylated for 10 minutes, treated 0.3% Triton X-100 for 20 minutes, and washed three times with PBS for 5 minutes each. Prehybridization was performed for 1 hour at 65°C with hybridization buffer without probe and then hybridization was done at 65°C overnight in a new hybridization buffer containing one of the DIG-labeled RNA probes. The hybridization buffer consisted of 5× saline sodium citrate (SSC; Gibco BRL/Invitrogen, Tokyo, Japan), 50% deionized formamide (Sigma, St. Louis, MO), 500 μg/ml herring sperm DNA (Roche), 5× Denhardt's solution (Open Biosystems, Huntsville, AL), and 250 μg/ml transfer RNA (Roche). After hybridization, the sections were sequentially treated with 2× SSC/50% formamide for 30 minutes at 65°C, 2× SSC for 30 minutes at 65°C twice, and 0.2× SSC for 5 minutes at room temperature. The hybridized probe was detected with an alkaline phosphatase-conjugated anti-DIG antibody using a DIG nucleic acid detection kit (Roche) according to the manufacturer's protocol.

Behavioral Tests

All behavioral experiments were performed with 2- to 3-month-old male mice with a mixed 129/Ola-C57BL/6 genetic background and in the light phase of their diurnal cycle, between 09:00 and 17:00 hours. All experimental protocols were approved by the Animal Care Committee of the Tohoku University School of Medicine, and all experiments were performed in compliance with the relevant laws and institutional guidelines.

Open Field Test

Mouse locomotor activity in the open field was measured using a photo-beam system (BTA-1, Muromachi-Kikai, Tokyo, Japan). The values for ambulation distance were accumulated for 30 minutes and logged onto a personal computer.

Step-Through Passive Avoidance Test

The learning ability of the mice was evaluated using a step-through passive avoidance memory test, as previously described.[28] The training apparatus was a box consisting of a small lighted compartment (15 × 10 × 10 cm^3) and a large dark compartment (18 × 12 × 10 cm^3). A 10 × 10 cm^2 guillotine door separated the two compartments. The light compartment was made of clear Plexiglas, and was illuminated by a lamp (60 W) from the outside. The dark compartment had a series of stainless-

steel rods (3 mm in diameter, 1 cm apart) through which a constant electrical current could be delivered. The mice were first habituated to the box on 2 consecutive days. On the first day, they were placed in the light compartment and allowed to explore the box. The latency period for entering the dark compartment was recorded. As soon as a mouse entered the dark compartment, the door was closed, and the mouse was kept inside for 15 seconds before being returned to its cage. On the second training day, on entry into the dark compartment, the mice were given 0.5 mA of current for 5 seconds. The test session was performed 24 hours after the training session using the same paradigm, but without the foot shock. The latency period for each mouse to move into the dark compartment was recorded for up to a maximum of 300 seconds.

Wire Hanging Test

The ability of mice to hang upside down from a wire screen was tested as previously described.[29] The wires were 1 mm in diameter and spaced 1 cm apart. A rectangular area of the screen was taped off to confine the mouse to an 18 × 26 cm section of the screen. After a mouse was placed on the screen, the screen was waved gently in the air three times to force the mouse to grip the wires. The screen was then immediately turned upside down, 70 cm above a large rodent housing cage. The latency period for the mouse to fall into the cage was recorded. Mice that did not fall during the 60-second trial period were removed and given a maximal score of 60 seconds.

Forced Swimming Test

Mice were individually forced to swim in an aquarium (25 × 40 × 20 cm) containing 15-cm-deep water at 25 ± 1°C; the total duration of mouse immobility was measured during a 6-minute test.[30] Each mouse was judged to be immobile when it ceased struggling and remained floating motionless in the water, making only those movements necessary to keep its head above water.

Footprint Analysis

Footprint assessment was performed to detect gait abnormalities that could contribute to deficits in motor coordination on land.[31] Each hindpaw was colored black and forepaw red using nontoxic dye. For each mouse, five or more consecutive strides were averaged.

Results

Expression of Hrs in Mouse Brain

We first performed *in situ* hybridization to examine the expression of the *hrs* gene in the central nervous system because currently there is no antibody to reliably detect Hrs in brain tissue. In 5-week-old wild-type mice, *hrs* was ubiquitously expressed in the brain, with higher expression in the hippocampus, cerebral cortex, and hypothalamus (Figure 1, A and F). The degree of expression was higher in the CA3 than in the CA1 subfield in the hippocampus (Figure 1, B and C). Distinct expression was seen in the Purkinje cells (Figure 1, D and E).

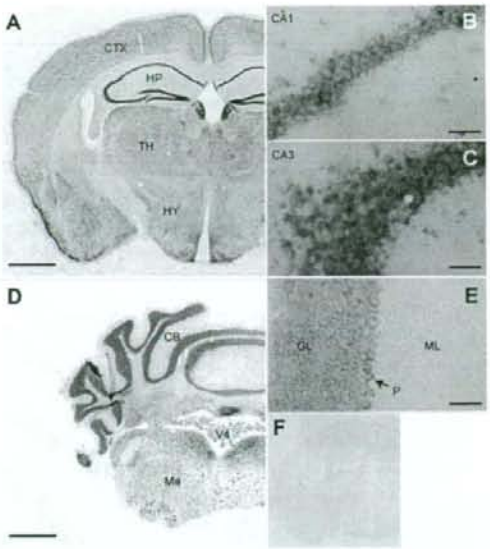

Figure 1. *In situ* hybridization of 5-week-old wild-type mouse brain probed for *hrs* mRNA. **A:** Coronal section through the cerebrum (hippocampus) showing the ubiquitous expression of *hrs* mRNA. Stronger *hrs* expression was seen in the CA3 (**C**) than the CA1 (**B**) subfield. **D** and **E:** Coronal section through the cerebellum showing strong expression of *hrs* in the granular cell layers and Purkinje cells. **F:** *In situ* hybridization of the section consecutive to **A** with the sense probe as a negative control. CTX, cerebral cortex; HP, hippocampus; TH, thalamus; HY, hypothalamus; CB, cerebellum; V4, fourth ventricle; Me, medulla oblongata; GL, granular layer; P, Purkinje cell; ML, molecular layer. Scale bars: 1 mm (**A**, **D**); 50 μm (**B**, **C**, **E**). Original magnifications: ×40 (**A**, **D**); ×400 (**B**, **C**, **E**).

Deletion of Hrs in the Central Nervous System

An *hrs* flox mouse was generated with *loxP* sites flanking exons 2 to 4 of the mouse *hrs* locus (Figure 2A). Heterozygous *hrs* flox ES cells were identified by Southern blot analysis (Figure 2B). To delete *hrs* specifically in the mouse brain, homozygous *hrs* flox mice ($hrs^{loxP/loxP}$) were crossed with *Synl-cre* transgenic mice. To assess whether exons 2 to 4 were deleted, we performed RT-PCR analysis of the brains from $hrs^{loxP/loxP}$;*Synl-cre*, and $hrs^{+/+}$;*Synl-cre* mice. A pair of primers spanning exons 1 and 7, respectively, amplified a 491-bp fragment from the $hrs^{+/+}$;*Synl-cre* brain and a 237-bp fragment from the $hrs^{loxP/loxP}$;*Synl-cre* brain (Figure 2C). Sequence analyses of the RT-PCR fragments showed that the *hrs* mRNA transcript from the $hrs^{loxP/loxP}$;*Synl-cre* brain contained a deletion of nucleotides 74 through 327, resulting in a frameshift and a stop codon in exon 5 (data not shown). PCR analyses of the genomic DNA from these brains revealed 0.3-kbp fragments (Figure 2D). Moreover, im-

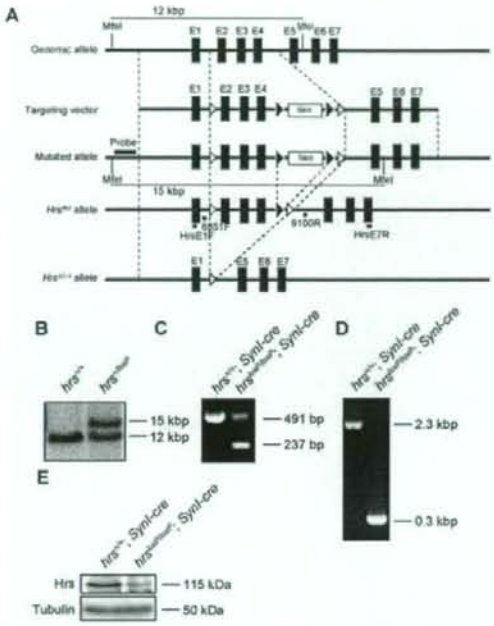

Figure 2. Generation of floxed *hrs* mice. **A:** Schematic representation of the *hrs* genomic locus, targeting vector, and *hrs* mutated locus. The targeting vector was designed to replace exon 2 (E2) to E4, which encode Hrs amino acids 74 to 327. The expected fragments generated by *MfeI* digestion were 12 and 15 kb for the wild-type and mutated alleles, respectively. **Open** and **closed arrowheads** denote the positions of the *loxP* and *FRT* sequences, respectively. **B:** Southern blot analysis of the *hrs* mutation in ES cell clones. DNA was digested with *MfeI*, and the blot was probed with the flanking 5′ probe as shown in **A**. Lines indicate the positions of the DNA fragments corresponding to the wild-type and mutated alleles. **C:** RT-PCR analysis of the total RNA from the brains of $hrs^{+/+}$;*Synl-cre* and $hrs^{loxP/loxP}$;*Synl-cre* mice. The primers used were HrsE1F and HrsE7R (see Materials and Methods). **D:** Genomic PCR analysis of the $hrs^{+/+}$;*Synl-cre* and $hrs^{loxP/loxP}$;*Synl-cre* brains. The primers used were 6851F and 9100R (see Materials and Methods). **E:** Western blot analysis for Hrs. Lysates from $hrs^{+/+}$;*Synl-cre* and $hrs^{loxP/loxP}$;*Synl-cre* brains were separated by sodium dodecyl sulfate-polyacrylamide gel electrophoresis and blotted with an anti-Hrs antibody.

munoblotting analysis with an anti-Hrs mAb revealed that ~60% of the Hrs expression was suppressed in the $hrs^{loxP/loxP}$;*Synl-cre* brain (Figure 2E). Because *Synl-cre* transgenic mice specifically express Cre recombinase in differentiated neurons, and not in astroglia,[20] these data suggest that both neurons and glial cells express Hrs. We conclude that the *hrs* flox allele represents a functional conditional allele.

Loss of Weight in Hrs Mutant Mice

$Hrs^{loxP/loxP}$;*Synl-cre* mice were morphologically indistinguishable from their littermates at birth. $Hrs^{+/+}$;*Synl-cre*, $hrs^{+/loxP}$;*Synl-cre*, and $hrs^{loxP/loxP}$;*Synl-cre* mice were obtained at the expected Mendelian ratios and were viable at least for several months. $Hrs^{+/loxP}$;*Synl-cre* mice did not differ in growth or behavior from their $hrs^{+/+}$;*Synl-cre* littermates. However, growth retardation of the $hrs^{loxP/loxP}$;*Synl-cre* mice became detectable by 3 weeks of age and gradually worsened; most of the $hrs^{loxP/loxP}$;*Synl-cre* mice did not show any increase in their body weight after they reached 8 weeks of age (Figure 3). Moreover, the $hrs^{loxP/loxP}$;*Synl-cre* mice were infertile.

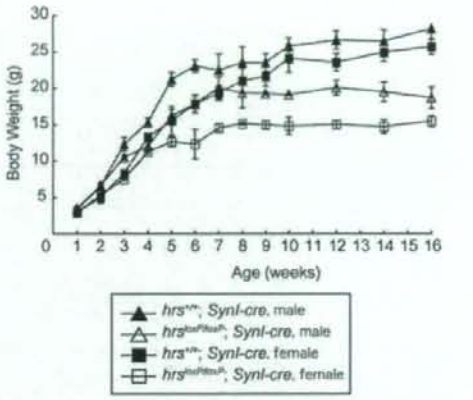

Figure 3. Phenotypes of the $hrs^{loxP/loxP}$;*Synl-cre* mice. Growth curves for $hrs^{+/+}$;*Synl-cre* (males, $n = 12$; females, $n = 9$) and $hrs^{loxP/loxP}$;*Synl-cre* (males, $n = 10$; females, $n = 9$) mice. Error bars indicate SE.

Loss of Pyramidal Neurons in the Hippocampal CA3 Subfield in Hrs Mutant Mice

We next performed histopathological examinations of the $hrs^{+/+}$;*Synl-cre* and $hrs^{loxP/loxP}$;*Synl-cre* mice by Nissl staining with cresyl violet. The gross anatomy of the Hrs mutant brain was normal. In the 2- and 3-week old brains, no histopathological difference was observed between the $hrs^{+/+}$;*Synl-cre* and $hrs^{loxP/loxP}$;*Synl-cre* mice (Figure 4, A–D). However, the number of pyramidal neurons in the hippocampal CA3 subfield was reduced in the 5-week-old $hrs^{loxP/loxP}$;*Synl-cre* brain (Figure 4, E and F), and progressive decreases were observed in the 8- and 28-week-old $hrs^{loxP/loxP}$;*Synl-cre* brains (Figure 4, G–J). In contrast, we could not detect any decrease in the pyramidal neurons in CA1. No difference was observed in any other regions, including the cerebral cortex, substantia nigra, striatum, cerebellum, or hypothalamus by Nissl staining or H&E staining (data not shown).

Immunostaining for the glial marker GFAP (glial fibrillary acidic protein) showed increased GFAP in the hippocampal CA3 subfield of the $hrs^{loxP/loxP}$;*Synl-cre* mice, suggesting the presence of neural damage in this region (Figure 5, A and B). To determine whether the reduced number of neurons observed in the $hrs^{loxP/loxP}$;*Synl-cre* mouse brain was caused by cell death, we performed TUNEL staining, which detects the DNA fragmentation in dying cells. Several TUNEL-positive cells were detected in the hippocampal CA3 subfield of 5-week-old $hrs^{loxP/loxP}$;*Synl-cre* mice, but no TUNEL-positive cells were detected in the $hrs^{+/+}$;*Synl-cre* hippocampus (Figure 5, C and D). These results suggest that neural cell death occurs in a specific brain region of the $hrs^{loxP/loxP}$;*Synl-cre* mice, the hippocampal CA3 subfield.